Gondwana Research xxx (xxxx) xxx

Contents lists available at ScienceDirect

Gondwana Research

journal homepage: www.elsevier.com/locate/gr

Flood detection using PolSAR decomposition, feature selection, and deep learning

Jinwook Lee [a], Saeid Janizadeh [a], Alexander Melancon [b], Sayed M. Bateni [a,c], Dongkyun Kim [d], Andrew Molthan [e], Changhyun Jun [f,*], Ramin Farhadiani [g], Saeid Homayouni [g], Megersa Dinka [h]

[a] Department of Civil, Environmental, and Construction Engineering and Water Resources Research Center, University of Hawaii at Manoa, Honolulu, HI 96822, USA
[b] Earth System Science Center, University of Alabama in Huntsville, Huntsville, AL 35805, USA
[c] UNESCO-UNISA Africa Chair in Nanoscience and Nanotechnology College of Graduate Studies, University of South Africa, Muckleneuk Ridge, Pretoria 0003, South Africa
[d] Department of Civil and Environmental Engineering, Hongik University, Seoul 04066, Republic of Korea
[e] Earth Science Branch, NASA Marshall Space Flight Center, Huntsville, AL 35812, USA
[f] School of Civil, Environmental and Architectural Engineering, Korea University, Seoul 02841, Republic of Korea
[g] Centre Eau Terre Environnement, Institut National de la Recherche Scientifique, Quebec City, Quebec G1K 9A9, Canada
[h] Department of Civil Engineering Science, Faculty of Engineering and the Built Environment, University of Johannesburg, Johannesburg 2006, South Africa

ARTICLE INFO

Keywords:
Flood detection
UAVSAR
Decomposition
Feature selection
Deep learning

ABSTRACT

Accurate identification of inundated areas is crucial for mitigating the impacts of flooding, which causes numerous casualties and significant economic losses. While polarimetric synthetic aperture radar (PolSAR) data have been utilized to detect inundated regions, the information contained within PolSAR features remains severely underutilized. We introduce a novel approach that involves extracting a large number of PolSAR features through various PolSAR decomposition techniques, selecting the most important ones using the decision tree–recursive feature elimination (DT-RFE) method, and ultimately detecting inundation using a convolutional neural network (CNN) model. The hybrid DT-RFE–CNN model was trained and tested over a region in southeastern North Carolina during Hurricane Florence on September 18, 2018, using PolSAR features derived from the Uninhabited Aerial Vehicle Synthetic Aperture Radar (UAVSAR). In terms of flood-mapping efficacy, the DT-RFE–CNN model outperformed a CNN model that used only PolSAR data across all metrics in both the training and testing stages. The performance of the trained DT-RFE–CNN model was evaluated by testing it over the same region for four more days (September 19, 20, 22, and 23, 2018); it achieved an average accuracy, precision, recall, F1 score, and intersection-over-union of 0.9304, 0.9089, 0.9584, 0.9324, and 0.8738, respectively, outperforming both the classical Otsu method and the FT-Transformer model using features selected by DT-RFE. Finally, we assessed the model's generalizability by mapping another significant flood event, caused by Hurricane Harvey in Texas between August and September 2017. Based on the results, the hybrid model can accurately detect flooding, even in regions on which it has not been trained. Thus, the proposed method can facilitate flood monitoring and response efforts.

1. Introduction

Flooding is one of the deadliest forms of natural disasters globally, causing numerous casualties and significant economic losses (Liang and Liu, 2020). Recently, an increasing population density near rivers, climate change, increasing rainfall, and rising sea levels have heightened the threat of flood damage even further (Tellman et al., 2021). According to a 2021 report by National Oceanic and Atmospheric Administration (Sweet et al., 2021), the frequency of typical damage-causing floods is expected to increase more than tenfold by 2050, and this could be exacerbated by regional factors. The report also highlights that without the implementation of additional risk-reduction measures, coastal infrastructure, communities, and ecosystems will become more vulnerable and be impacted more severely. Thus, the potential economic

* Corresponding author.
E-mail address: cjun@korea.ac.kr (C. Jun).

https://doi.org/10.1016/j.gr.2025.06.022
Received 30 January 2025; Received in revised form 11 May 2025; Accepted 22 June 2025
Available online 17 July 2025

impact on flood-prone communities underscores the urgent need for adaptive measures to mitigate flood risk and damage.

Hurricane-induced floods have resulted in significant losses in terms of infrastructure and human life. For instance, in 2017, Hurricane Harvey caused excessive rainfall in the densely populated Houston metropolitan area of Texas, flooding over 300,000 buildings and approximately 500,000 vehicles (Martinaitis et al., 2021). The hurricane affected 13 million people and destroyed over 100,000 homes, resulting in economic losses of approximately $125 billion (Blake and Zelinsky, 2018; Shultz and Galea, 2017). In 2018, Hurricane Florence caused flooding in North Carolina (NC), leading to 22 direct fatalities in the United States (Stewart and Berg, 2019) and approximately $24 billion in damages (Callaghan, 2020). In 2024, Hurricane Helene triggered catastrophic flooding in the southeastern United States, resulting in 219 fatalities and an estimated $79.5 billion in damages (Smith, 2025).

One of the major challenges when responding to flooding is accurately defining the extent of the affected area to gain an overall perspective of the incident (Rahman and Thakur, 2018). Accurate mapping of flood extent provides essential baseline information, facilitating informed decision-making and the development of effective plans for flood mitigation efforts (Mohammadi et al., 2017). In essence, accurate flood inundation mapping over large areas is a critical initial step in flood disaster management programs and rapid-response operations post flood disasters, allowing resources to be allocated to affected areas (Schumann et al., 2018). Additionally, identifying inundated areas is necessary for generating flood vulnerability, risk, and hazard maps, which are vital for disaster management authorities (Mahmoud and Gan, 2018; Swain et al., 2020). The value of this information is realized when details about the inundated areas are shared in time with the authorities (Manavalan, 2017). With weather anomalies occurring more frequently, detecting inundated areas faster and more accurately is imperative for effective disaster response (Uddin et al., 2021). Inaccurate flood detection leads to unreliable flood vulnerability, risk, and hazard maps, ultimately impairing the capacity to forecast, prepare for, respond to, and recover from floods (Razavi-Termeh et al., 2023). Hence, accurate flood detection methodologies represent a critical necessity for effectively mitigating the growing risks associated with floods.

Remote sensing (RS) technology is being increasingly utilized for flood monitoring as it offers the capability to observe spatial distribution at high temporal resolutions (Brivio et al., 2002; Lee et al., 2023; Rättich et al., 2020; Sun et al., 2017). Regarding flood events, RS technology is crucial, especially during the response phase, as it can provide the information necessary for mapping and monitoring flood areas in a cost-effective and timely manner (Amitrano et al., 2018; Martinis et al., 2015). Studies have utilized various optical satellites for flood detection (Alganci et al., 2019; Fayne et al., 2017; Güvel et al., 2022; Mehmood et al., 2021). However, poor weather conditions, such as clouds, rain, and fog, can impact optical sensors, precluding the production of high-quality images (Musa et al., 2015). Moreover, optical satellites cannot detect water in areas covered by vegetation (Musa et al., 2015). Additionally, optical satellites that utilize visible light can be operated only during the day as they rely on solar radiation reflection (Manavalan, 2017; Melancon et al., 2021; Musa et al., 2015).

Synthetic aperture radar (SAR) is widely acknowledged as a viable solution to the aforementioned problems (Manavalan, 2017; Rahman and Thakur, 2018; Sun et al., 2017). Unlike optical sensors that passively detect color characteristics based on the absorption and reflection of visible light, SAR actively emits microwaves and measures the reflected signals (Sommervold et al., 2023). Additionally, while optical sensors cannot monitor the land surface in cloudy conditions, SAR can operate under all weather conditions, penetrating visual obstructions such as clouds and fog (McNairn and Shang, 2016; Wang et al., 2019). SAR sensors operate at various frequencies, including the L-, C-, and X-bands corresponding to wavelengths of 24, 5.66, and 3 cm, respectively (Adeli et al., 2021). In general, longer wavelengths are more effective in penetrating vegetation, enabling the detection of floodwaters beneath forest canopies (Pierdicca et al., 2018). This capability makes SAR particularly valuable for continuous monitoring and time-sensitive applications (Edrich, 2004), enabling real-time assessment of flooded areas regardless of weather conditions or time of day (Chapman et al., 2015; Clement et al., 2018; Manavalan, 2017; Moreira et al., 2013; Musa et al., 2015).

Various studies have demonstrated the effectiveness of SAR in mapping surface water (Kavats et al., 2022; Pham-Duc et al., 2017), wetlands (Adeli et al., 2020; White et al., 2015), flood extent (Long et al., 2014; Ouled Sghaier et al., 2018), vegetation (Furtado et al., 2016), land cover (Waske and Braun, 2009), and snow cover (He et al., 2017; Tsai et al., 2019). Among various SAR bands, the L-band is known to be particularly effective in mapping and identifying inundated areas (Martinis and Rieke, 2015; Ramsey III et al., 2013; Richards et al., 1987; Wang and Imhoff, 1993). In addition, the Uninhabited Aerial Vehicle Synthetic Aperture Radar (UAVSAR) provides data with a spatial resolutions finer than 10 m, offering greater detail than open-access optical satellite data such as Sentinel-2 and Landsat 8 (Fore et al., 2015; Huang et al., 2021; Phang et al., 2023).

The simplest approach for flood area mapping involves applying a certain threshold to the SAR backscatter values (Manavalan, 2017). Various studies have employed SAR data with the threshold method to map inundated regions across different scales, utilizing the characteristic low backscatter from open water surfaces (Costa, 2004; Guo, 2000; Liu et al., 2002; Matgen et al., 2011; Rahman and Thakur, 2018; Schumann et al., 2010; Song et al., 2007; Yamada, 2001). An appropriate threshold is manually determined through trial and error by visually inspecting the image histogram in a supervised manner (Manavalan, 2017). However, careful attention is required in flood mapping from SAR images as some areas, such as high-altitude regions, shadows, runways, and extensive road networks, may show similar reflectance to inundated regions (Manavalan, 2017). Furthermore, challenges such as speckle noise and uneven grayscale distribution in SAR images often cause traditional methods to fall short of the requirements for large-scale applications (J. Wang et al., 2022). Thus, the integration of SAR data with advanced flood inundation mapping algorithms is becoming increasingly necessary.

Polarimetric synthetic aperture radar (PolSAR) systems transmit electromagnetic waves in various polarization states, providing more information than conventional SAR systems (Aghababaee and Sahebi, 2018; Pallotta and Orlando, 2018). To enhance the classification accuracy for ground objects, extracting their features from PolSAR data is crucial (Li et al., 2018; Liu et al., 2022; Zhang et al., 2021). PolSAR decomposition, also frequently referred to more broadly as polarimetric decomposition, is a widely used technique for analyzing scattering mechanisms and extracting features from ground objects (Richards, 2009). The application of features derived from PolSAR decomposition often leads to superior mapping outcomes compared with those achieved using conventional SAR data alone. For example, PolSAR decompositions have been used for vegetation mapping (Furtado et al., 2016), urban mapping (Duan et al., 2021), the mapping of plant functional types in wetlands (Morandeira et al., 2016), and land cover classification (Khosravi et al., 2018; Zhao and Jiang, 2022). The primary objective of PolSAR decompositions is to distinguish backscattered signals based on the scattering mechanism. Although PolSAR features (also referred to more broadly as polarimetric features) have been used in various applications (Duan et al., 2021; Furtado et al., 2016; Han et al., 2020; Khosravi et al., 2018; Morandeira et al., 2016; Zhang et al., 2024; Zhao and Jiang, 2022), the implicit information contained in them has yet to be utilized for flood mapping. Polarimetric decompositions are crucial as they can directly enhance flood detection. Numerous polarimetric decomposition models have been introduced to investigate scattering parameters (Lee and Pottier, 2017). The outcomes of polarimetric decomposition have a significant impact on subsequent applications (Chen et al., 2023). Consequently, employing polarimetric

decomposition methods that can efficiently and accurately extract features from ground objects is crucial.

Recently, the combination of machine learning (ML) with SAR and PolSAR data has been gaining increasing attention in the realm of flood inundation mapping (Bentivoglio et al., 2022; Verma et al., 2023; J. Wang et al., 2022). Studies have leveraged the advantages of various ML-based image classification approaches, primarily by integrating multiple image-processing functions to distinguish inundated pixels from other pixels with similar reflectance, thereby enhancing mapping accuracy (Karim et al., 2023). In these methods, ML-based approaches are trained using available reference flood maps to recognize classification parameters. Notably, the development of ML techniques such as random forest, support vector machine (SVM), and convolutional neural network (CNN) has significantly facilitated the processing of large volumes of multi-temporal SAR data (Banks et al., 2019; Chen et al., 2018; Mahdianpari et al., 2017; Nemni et al., 2020; Thanh Noi and Kappas, 2018). Among ML techniques, CNNs are renowned for their performance in image recognition tasks and are widely used in vegetation mapping (Sun et al., 2023), flood detection (Andrew et al., 2023), land cover classification (Wang et al., 2015), and forest monitoring (Brovelli et al., 2020) based on SAR data. However, the identification of the most suitable PolSAR features is widely recognized as a crucial prerequisite for implementing CNNs (Plank et al., 2017).

The derivation of PolSAR features using various decomposition methods and their optimal selection using a robust ML technique are significantly advantageous in flood mapping. When combined with a CNN model, PolSAR features could be valuable for accurate flood mapping. Accordingly, this study introduces a novel approach for flood detection using L-band fully polarized PolSAR images obtained from Uninhabited Aerial Vehicle Synthetic Aperture Radar (UAVSAR). First, multiple decomposition techniques, such as Freeman–Durden decomposition (Freeman and Durden, 1998) and H/A/Alpha decomposition (Cloude and Pottier, 1997), are utilized to generate 100 PolSAR features from PolSAR data. Subsequently, the decision tree–recursive feature elimination (DT-RFE) algorithm is used to select the most important features, which enhances the model's efficiency in distinguishing between flood and non-flood areas. Finally, a CNN model is employed for high-resolution flood segmentation to intricately map flood inundation. The model is trained and tested over a flight path across the Lumber River in the southeastern region of North Carolina during Hurricane Florence on September 18, 2018. Then, it is evaluated over the same region on four more dates (September 19, 20, 22, and 23, 2018). Finally, the model's generalizability is validated by mapping floods caused by Hurricane Harvey in Texas on August 31 and September 2, 2017.

2. Study area and data

2.1. Study area

This study focused on Hurricane Florence, which impacted southeastern NC in September 2018. Hurricane Florence was an intense, long-lasting hurricane that triggered substantial devastation in Carolina, predominantly due to surface water flooding from heavy rains (Feaster et al., 2018). It began as a robust tropical wave emerging from the west coast of Africa on August 30, 2018. On September 11, it reached its peak intensity, with winds of 67 m/s, becoming a Category 4 hurricane on the Saffir–Simpson scale as it crossed the Atlantic (Stewart and Berg, 2019).

Florence made landfall as a Category 1 hurricane immediately south of Wrightsville Beach, North Carolina, on September 14 (Feaster et al., 2018). Thereafter, the forward speed of the hurricane decreased to about 1.0 m/s, resulting in over 90.0 cm of rain in the southeastern region of North Carolina for four days, which caused extensive flooding. Hurricane Florence caused 22 direct fatalities across the United States (Stewart and Berg, 2019). The National Center for Environmental Information estimates that Florence caused around $24 billion in damage from flooding and winds, which ranks it as the ninth most destructive hurricane to strike the United States (Callaghan, 2020).

Fig. 1 shows maps of the study area in North Carolina—including the annual land use in 2018—generated by the Landscape Change Monitoring System (LCMS) (U.S. Department of Agriculture, 2024), along with an elevation map from the Shuttle Radar Topography Mission (SRTM) (NASA JPL, 2013). The study area covers a specific UAVSAR flight path along the Lumber River in southeastern North Carolina. The area is located in the lower coastal plain; the river traverses the coastal plain, flowing into the Atlantic Ocean. According to the Köppen climate classification, the region falls under the humid subtropical climate category (Rubel and Kottek, 2010). Summers are hot and extremely humid, while winters are cool, with occasional, brief cold spells (Wang et al., 2022). During the Atlantic hurricane season, tropical cyclones can cause extreme rainfall events, potentially triggering severe flooding disasters, particularly during the peak period, i.e., mid-August to mid-October (Sayemuzzaman and Jha, 2014).

The inner coastal plains of North Carolina are mostly flat, with a gradual decline in elevation toward the Atlantic Ocean. The local landscape is characterized by dominant land cover types comprising agriculture fields and forests (Wang et al., 2022). Considering the abundant vegetation in the study area, much of the flooding could be hidden in visible imagery, which may reduce the effectiveness of flood mapping efforts (Melancon et al., 2021).

2.2. UAVSAR data

UAVSAR comprises a PolSAR unit mounted on an aerial vehicle to acquire data repetitively over a defined path of interest. The vehicle is a NASA Gulfstream-III jet featuring an onboard navigation system based on real-time GPS to ensure the aircraft stays within 10 m of its planned flight path (Lou, 2022; Melancon et al., 2021). UAVSAR uses a quad-pol L-band SAR unit operating at a frequency of 1.26 GHz, with viewing angles of 25–60° (Rosen et al., 2007). The SAR sensors operate in the L (24 cm wavelength), C (5.66 cm wavelength), and X (3 cm wavelength) bands (Adeli et al., 2021). The relatively longer wavelength of the L-band enables deeper penetration and better identification of ground terrain, allowing the sensors to map and identify more inundated areas than those in the other bands (Martinis and Rieke, 2015; Ramsey III et al., 2013; Richards et al., 1987; Wang and Imhoff, 1993). Moreover, PolSAR (or quad-pol SAR) sensors, which can transmit and receive four types of signals, enable the analysis of diverse scattering mechanisms generated by interactions of the electromagnetic waves with surface objects (Babu et al., 2020; Melancon et al., 2021; Tsyganskaya et al., 2018; Ullmann et al., 2016; White et al., 2015).

NASA conducted UAVSAR flights over several key river basins in North Carolina from September 17 to 23, 2018, with up to six revisits as a reaction to Hurricane Florence. The UAVSAR data portal (https://uavsar.jpl.nasa.gov/cgi-bin/data.pl) provides access to the generated dataset (Jet Propulsion Laboratory, 2023). Considering proximity and observation frequency, we directed our attention to a specific flight path (ID: lumber_31509) across the Lumber River. The study area is hereinafter referred to as the "Lumber flight path."

The PolSAR sensors installed on UAVSAR send and collect signals in four combinations of horizontal and vertical directions, providing components for four polarizations. Each pixel contains signal strength and phase details and is stored in a complex form. These pixels can be conveniently described using a complex scattering matrix **S**, which is expressed as:

$$\mathbf{S} = \begin{bmatrix} S_{HH} & S_{HV} \\ S_{VH} & S_{VV} \end{bmatrix} \quad (1)$$

where S is the polarized electromagnetic wave. In the subscript, the first and second letters represent the polarizations of the transmitted and received signals, respectively. V and H respectively denote the vertical and horizontal polarizations of the electromagnetic wave. S_{HH}, S_{HV}, S_{VH},

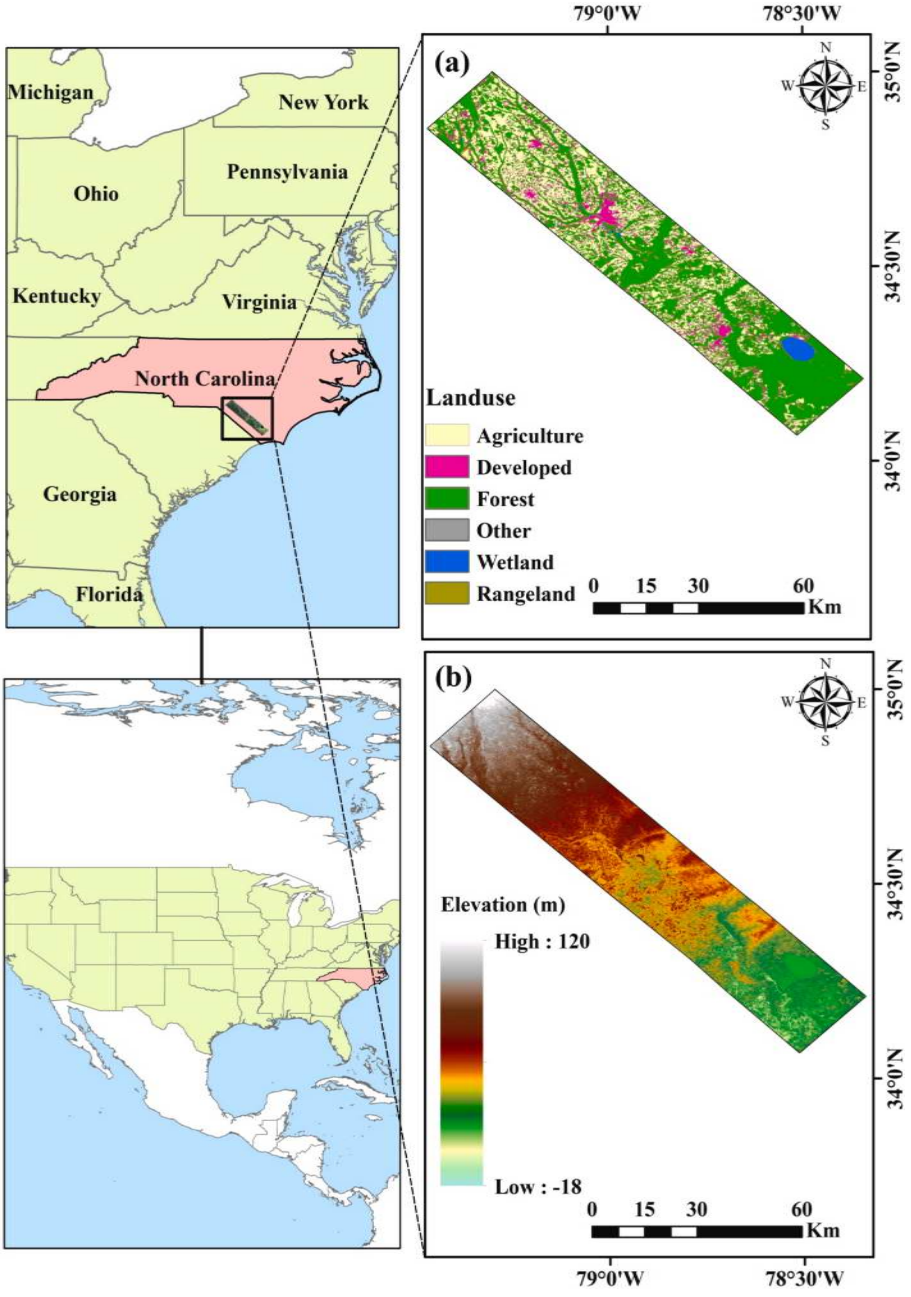

Fig. 1. Study area in North Carolina: (a) land use and (b) elevation.

and S_{VV} are referred to as single-look complex (SLC) products and are not available in most regions, including our study area.

However, multi-look complex (MLC) products and ground range detected (GRD) products are available for our study area. MLC products are generated from SLC files by averaging multiple looks to reduce noise and enhance data quality before classification (Cantalloube and Nahum, 2000; Melancon et al., 2021). GRD products are calibrated complex cross-products from MLC products that are mapped onto the ground using basic geographic coordinates (Jet Propulsion Laboratory, 2015). Both MLC and GRD products include a total of six elements: three real floating-point files with four bytes per pixel (i.e., $S_{HH}S^*_{HH}$, $S_{HV}S^*_{HV}$, and$S_{VV}S^*_{VV}$) and three complex floating-point files with eight bytes per pixel (i.e., $S_{HH}S^*_{HV}$, $S_{HH}S^*_{VV}$, and$S_{HV}S^*_{VV}$), where S^* represents a conjugate complex number. Eventually, GRD products are used to create the covariance matrix (C3) or coherency matrix (T3) for PolSAR decompositions. In this study, we employed GRD products as the PolSAR data.

2.3. UAVSAR false-color red, green, and blue (RGB) image

To obtain sample flood and non-flood polygons over the study area, we generated a UAVSAR false-color RGB image of the study area. Fig. 2 shows the location of the Lumber flight path (our study area) within southeastern North Carolina. Following the technique employed by Melancon et al. (2021), we created a UAVSAR false-color RGB image for September 18, 2018, via Freeman–Durden decomposition (Freeman and Durden, 1998), which is one of the most popular PolSAR decompositions (Fig. 2) and is widely used for analyzing SAR data (Ballester-Berman and Lopez-Sanchez, 2010). It helps differentiate the manners in which radar signals interact with surfaces, simplifying the interpretation of the scattering patterns seen in radar images (An and Lin, 2019). This technique plays a key role in understanding how radar waves reflect off

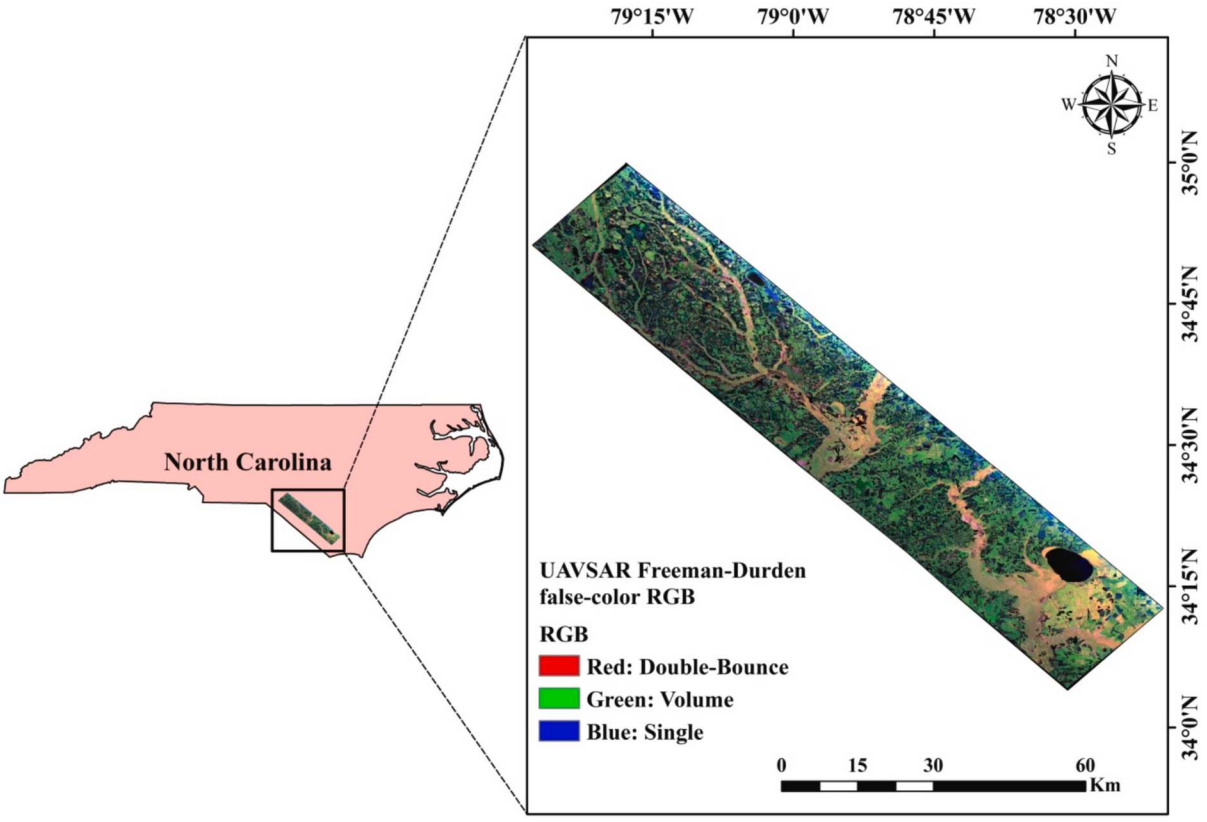

Fig. 2. Location of Lumber flight path in North Carolina and corresponding UAVSAR false-color RGB image for September 18, 2018.

various features on the ground, such as buildings, forests, or water. Freeman–Durden decomposition, can separate these interactions into three main types of scattering, each linked to different physical processes (Han et al., 2018).

The Freeman–Durden method produces three arrays, each corresponding to a specific scattering mechanism that matches the intensity of the backscatter patterns in the radar image (Freeman and Durden, 1993). In false-color RGB representations of Freeman–Durden decompositions, these three scattering mechanisms are typically mapped to different color channels. The first channel (red) highlights double-bounce scattering, where radar signals bounce between two surfaces, such as between the ground and a building or tree trunk. The second channel (green) represents volume scattering, observed in more complex areas such as forests, where the radar signal bounces around within trees or vegetation. The third channel (blue) represents single scattering, which occurs on flat surfaces such as water or smooth terrain (Cui et al., 2012; Freeman and Durden, 1993; Q. Xie et al., 2018). In Fig. 2, the black-shaded area in the lower right part of the swath is a lake. The data from September 18, 2018, were used for both training and testing, while the data from the remaining dates were reserved exclusively for further external validation.

3. Methodology

3.1. Model development

The innovative hybrid approach for flood detection introduced in this study comprises the following five steps (Fig. 3):

(1) Data preprocessing: This involves obtaining PolSAR features through PolSAR decompositions, reducing speckle noise, and a

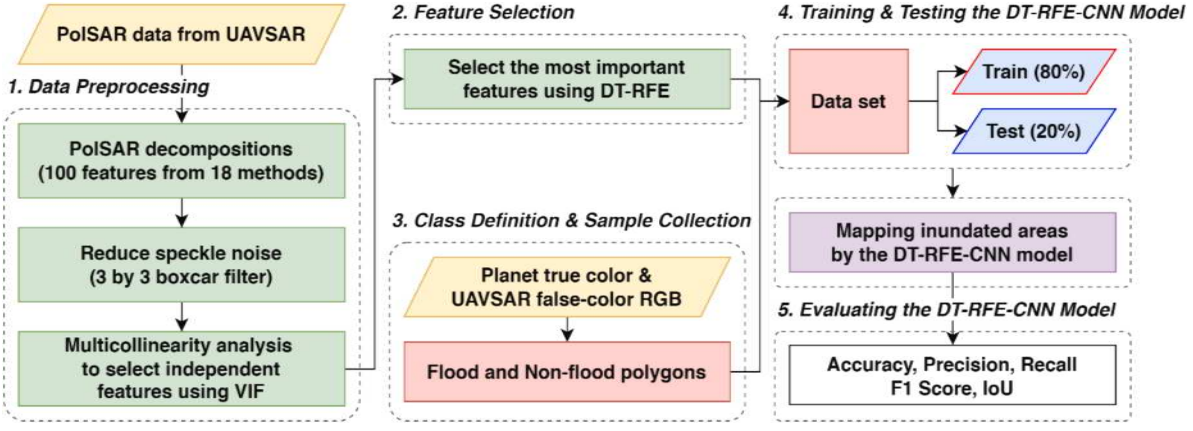

Fig. 3. Flowchart illustrating the hybrid PolSAR decomposition and DT-RFE–CNN model for flood mapping.

multicollinearity analysis of PolSAR features using the variance inflation factor (VIF). Details on PolSAR decomposition and speckle noise reduction are provided in Section 3.2, while the use of VIF for addressing multicollinearity is thoroughly covered in Section 3.3.

(2) Feature selection: The DT-RFE algorithm is used to select the most important PolSAR features to maximize the accuracy of detecting inundated regions. These features are then utilized as the input for the CNN model. Section 3.4 describes the DT-RFE algorithm in detail.

(3) Class definition and sample collection: Sample flood and non-flood polygons are obtained from visible imagery (namely, Planet true-color and UAVSAR false-color RGB images) for September 18, 2018. These sample polygons serve as the outputs of the CNN model. Details about flood and non-flood polygons are provided in Section 3.5.

(4) Training and testing of DT-RFE–CNN model: The input (PolSAR features from Step 2) and output (flood and non-flood polygons from Step 3) data for September 18, 2018, are divided into training and testing sets. The training dataset is utilized to train the DT-RFE–CNN model, while the testing dataset is used to assess its performance. The CNN is employed for high-resolution flood segmentation to intricately depict the extent of flooding, as described in Section 3.6. Furthermore, manually specified flood and non-flood pixels for the subsequent days (September 19, 20, 22, and 23, 2018) are employed for validation. Finally, the generalizability of the trained DT-RFE–CNN model is evaluated over a region in Texas for August 31 and September 2, 2017, during Hurricane Harvey.

(5) Evaluating the DT-RFE–CNN model: The performance of the hybrid model over different domains and days is evaluated based on five different metrics, namely accuracy, precision, recall, F1 score, and intersection-over-union (IoU). The expressions for these metrics are provided in Section 3.7.

3.2. PolSAR decompositions and speckle noise reduction

We used the PolSARPro v6.0 software to preprocess the PolSAR data from UAVSAR (Pottier, 2023). This software is equipped with all the modules needed for preprocessing data and creating PolSAR features. It is an open-source program created by the European Space Agency. It can utilize UAVSAR data to generate various PolSAR features using various PolSAR decomposition techniques.

The UAVSAR data for the study area were available in GRD format. The PolSAR data from UAVSAR represent calibrated multi-looks and are purely binary, without any header bytes. They were available in floating-point format with three 8-byte files ($S_{HH}S^*_{HV}$, $S_{HH}S^*_{VV}$, and $S_{HH}S^*_{VV}$) and three 4-byte files ($S_{HH}S^*_{HH}$, $S_{HV}S^*_{HV}$, and $S_{VV}S^*_{VV}$). These were used to derive the covariance matrix ($C3$), which is expressed as (Woodhouse, 2017):

$$C3 = \begin{bmatrix} \langle S_{HH}S^*_{HH}\rangle & \sqrt{2}\langle S_{HH}S^*_{HV}\rangle & \langle S_{HH}S^*_{VV}\rangle \\ \sqrt{2}\langle |S_{HH}|^2\rangle & 2\langle S_{HV}S^*_{HV}\rangle & \sqrt{2}\langle S_{HV}S^*_{VV}\rangle \\ \langle |S_{HH}|^2\rangle & \sqrt{2}\langle S_{HH}S^*_{VV}\rangle & \langle S_{VV}S^*_{VV}\rangle \end{bmatrix} \quad (2)$$

The primary objective of PolSAR decomposition is to differentiate backscatter signals based on their scattering mechanisms (Cloude and Pottier, 1996). Numerous PolSAR decompositions have been established to investigate scattering parameters (Lee and Pottier, 2017). These are generally divided into two categories: coherent and incoherent (Verma et al., 2023). Coherent decompositions are ideal for analyzing pure targets that yield complete polarimetric backscatter responses. Conversely, incoherent decompositions are better suited for examining distributed targets that produce partially polarized backscatter within a single SAR cell (Verma et al., 2023).

The Freeman–Durden decomposition (FRE3), introduced by Freeman and Durden (1998), was the first model-based PolSAR decomposition. This approach involves calculating three power components, which represent surface scattering, double-bounce scattering, and volume scattering. However, the double-bounce scattering model is designed specifically for tetrahedrons with a 0° orientation angle, which potentially renders it less effective for urban environments, where larger orientation angles are common (Chen et al., 2023).

To address the aforementioned issue, several models that fully characterize the scattering mechanisms of tetrahedrons with varying orientation angles have been proposed. Most of these models are derivatives of the basic dihedral model suggested for FRE3 (Freeman and Durden, 1998). Accordingly, the general four-component scattering power decomposition (SIN4) was suggested, which involves directly rotating the dihedral scattering model (Singh et al., 2013). Another approach involves transforming the measured coherency matrix, a notable example of which is the four-component decomposition (Y4O) (Yamaguchi et al., 2006). In certain urban areas with specific orientation angles, this decomposition method can amplify the proportion of double-bounce energy scattering (Yamaguchi et al., 2011). Building on the concept of rotating coherence matrices, advanced PolSAR decomposition techniques such as the six-component scattering decomposition (6SD) (Singh and Yamaguchi, 2018) and seven-component scattering decomposition (7SD) (Singh et al., 2019) have been proposed. Additionally, several recent studies have introduced model-based decompositions (M E and Kumar, 2020; Ramya and Kumar, 2021; Shafai and Kumar, 2020).

In this study, we aimed to extract PolSAR features using as many methods as possible, obtaining 100 PolSAR features from a total of 18 PolSAR decompositions. Moreover, following the method used by Xu et al. (2016) and Xie et al. (2018), a 3×3 sliding-window boxcar filter was used to reduce speckle noise. Table 1 details the PolSAR decomposition methods and the resulting PolSAR features used in this study.

3.3. Multicollinearity analysis

Multicollinearity arises when predictor variables in ML models exhibit a strong correlation with one another (Vatcheva et al., 2016). This can produce unstable coefficient estimates, reduce the clarity of model interpretation, and compromise predictive performance. To mitigate these challenges, evaluating the extent of multicollinearity among the 100 PolSAR features calculated in this study is essential. One widely used metric for assessing multicollinearity is VIF, which quantifies the increase in the variance of a regression coefficient due to collinearity among the predictors (O'brien, 2007).

A VIF of 1 indicates that no correlation exists between the predictor variable and other variables, signifying the absence of multicollinearity. VIF values between 1 and 5 suggest moderate correlation between variables, which is generally not concerning. A VIF exceeding 5 indicates strong correlation and potential multicollinearity issues that warrant further investigation. A VIF greater than 10 is considered a sign of severe multicollinearity that must be addressed (Kim, 2019; Vatcheva et al., 2016). Detailed information regarding VIF has been provided by Dormann et al. (2013) and Montgomery et al. (2021). In line with previous studies (James et al., 2023; Menard, 2001; Vittinghoff et al., 2012), we eliminated features with VIFs equal to or greater than 10.

3.4. DT-RFE

In ML and data analysis, feature selection is essential for enhancing model performance and interpretability (Saeys et al., 2007). DT-RFE is an effective feature selection approach that leverages the inherent ranking of feature importance based on DTs (Awad and Fraihat, 2023; Lian et al., 2020). By systematically removing less significant features, this method refines the feature set, improving the accuracy and efficiency of the model.

RFE is a wrapper-based feature selection technique that iteratively focuses on smaller subsets of features. The process starts with training a model on the entire feature set and ranking the features according to their significance to the model. The least important features are

Table 1
PolSAR decomposition techniques and resulting PolSAR features used in this study; the features are prefixed with the abbreviated method and feature name.

Decomposition technique (abbreviation)	Number of features	PolSAR features	Reference
Aghababaee (AGH)	19	Alphap_mean, Alphap_SM1, Alphap_SM2, Alphap_SM3, M_SM1, M_SM2, M_SM3, Orientation_max_mean, Orientation_max_SM1, Orientation_max_SM2, Orientation_max_SM3, Phip_mean, Phip_SM1, Phip_SM2, Phip_SM3, Tawp_mean, Tawp_SM1, Tawp_SM2, Tawp_SM3	Aghababaee and Sahebi (2018)
An & Yang-3 (AN3)	3	AN3_Odd, AN3_Dbl, AN3_Vol	An et al. (2010)
An & Yang-4 (AN4)	4	AN4_Odd, AN4_Dbl, AN4_Vol, AN4_Hlx	An et al. (2011)
Arii-3 ANNED (ANNED)	3	ANNED_Odd, ANNED_Dbl, ANNED_Vol	Arii et al. (2010)
Bhattacharya & Frery-4 (BF4)	4	BF4_Odd, BF4_Dbl, BF4_Vol, BF4_Hlx	Bhattacharya et al. (2015)
Freeman-2 (FRE2)	2	FRE2_Ground, FRE2_Vol	Freeman (2007)
Freeman-3 (FRE3)	3	FRE3_Odd, FRE3_Dbl, FRE3_Vol	Freeman and Durden (1998)
H/A/Alpha (HAA)	7	HAA_Entropy, HAA_Anisotropy, HAA_Alpha, HAA_Beta, HAA_Lambda, HAA_Gamma, HAA_Delta	Cloude and Pottier (1997)
Krogager (KRO)	4	KRO_Teta, KRO_Kd, KRO_Kh, KRO_Ks	Krogager (1990)
L. Zhang-5 (MCSM)	5	MCSM_Odd, MCSM_Dbl, MCSM_Vol, MCSM_Hlx, MCSM_Wire	Zhang et al. (2008)
Neumann (NEU)	3	NEU_Tau, NEU_Delta_NEU_Mod, NEU_Delta_pha	Neumann (2009)
Singh-4 (SIN4)	4	SIN4_Odd, SIN4_Dbl, SIN4_Vol, SIN4_Hlx	Singh et al. (2013)
Singh-Yamaguchi-6 (6SD)	6	6SD_Odd, 6SD_Dbl, 6SD_Vol, 6SD_Hlx, 6SD_OD, 6SD_CD	Singh and Yamaguchi (2018)
Singh-7 (7SD)	7	7SD_Odd, 7SD_Dbl, 7SD_Vol, 7SD_Hlx, 7SD_OD, 7SD_MD, 7SD_CD	Singh et al. (2019)
Touzi (TSVM)	16	TSVM_Alpha_s, TSVM_Alpha_s1, TSVM_Alpha_s2, TSVM_Alpha_s3, TSVM_Phi_s, TSVM_Phi_s1, TSVM_Phi_s2, TSVM_Phi_s3, TSVM_Psi, TSVM_Psi1, TSVM_Psi2, TSVM_Psi3, TSVM_Tau_m, TSVM_Tau_m1, TSVM_Tau_m2, TSVM_Tau_m3	Touzi (2007)
Van Zyl-3 (VZ3)	3	VZ3_Odd, VZ3_Dbl, VZ3_Vol	Van Zyl (1993)
Yamaguchi-3 (YAM3)	3	YAM3_Odd, YAM3_Dbl, YAM3_Vol	Cui et al. (2012)
Yamaguchi-4 (Y4O)	4	Y4O_Odd, Y4O_Dbl, Y4O_Vol, Y4O_Hlx	Yamaguchi et al. (2005)

subsequently discarded, and the model is then retrained. This cycle repeats until the optimal number of features remains (Guyon et al., 2002).

When implementing RFE, DT is used as the baseline model for evaluating feature importance. DTs are particularly suitable for this task because they inherently rank features based on their contribution to reducing impurity (such as Gini impurity or entropy) at each split in the tree. This ranking provides a straightforward mechanism to identify and eliminate the least important features (Awad and Fraihat, 2023).

The procedure is initialized with the full set of features in the dataset, using which a DT is initially trained. The importance of each feature is evaluated based on the trained model and is typically determined by the total reduction in a criterion that the feature contributes. The features are then ranked according to their importance, and the least significant ones are removed. The model is retrained on the reduced set of features, whereafter the remaining features are re-ranked. This process is iterated, with the least important features being eliminated at each step, until the desired number of features has been achieved (Awad and Fraihat, 2023; Kuhn and Johnson, 2013).

DT-RFE offers several advantages as DTs can capture complex, nonlinear relationships and interactions between features; thus, they are ideal for datasets with such characteristics. They naturally quantify feature importance, which simplifies the feature selection process. By eliminating irrelevant or redundant features, DT-RFE can improve a model's performance, mitigate overfitting, and reduce computational costs (Awad and Fraihat, 2023; Lian et al., 2020).

3.5. Training and testing data

Sample flood and non-flood polygons over the study area were obtained from visible imagery (namely, Planet true-color and UAVSAR false-color RGB images) for September 18, 2018. The Planet true-color image was provided by Planet Lab, which is the first private data provider to contribute to the International Charter on Space and Major Disasters. Planet Lab shares Planet true-color images (PlanetScope) with the public during disasters such as Hurricane Florence (Melancon et al., 2021). By offering timely access to satellite data, Planet facilitates disaster response efforts, ensuring more efficient coordination and aid deployment during critical events. The true-color image for the study area during Hurricane Florence on September 18, 2018, was sourced through the NASA Commercial Data Buy Pilot for FY19 (https://www.planet.com/disaster/). This image was captured by digital cameras installed on NOAA's King Air turboprop aircraft at altitudes of 500–1,500 m (Melancon et al., 2021; National Oceanic and Atmospheric Administration, 2024; Office of Marine and Aviation Operations, 2024). The Planet visible image along with the UAVSAR false-color RGB image were employed as references to detect sample flood and non-flood pixels.

To collect ground reference data for training and testing the CNN model, polygons representing flood and non-flood classes were manually digitized in ArcGIS 10.5 (Fig. 4). As illustrated, both the true-color image from Planet and the UAVSAR false-color RGB composite were used to generate flood and non-flood polygons. In creating these polygons, the scattering intensities for single, double-bounce, and volume scattering were analyzed across various land cover types. Flood pixels displayed a distinct color pattern in the false-color Freeman–Durden RGB composite, showing average RGB values of approximately 160 for red, 83 for green, and 46 for blue, which produced orange and pink hues. This color contrast is especially useful for identifying floodwaters, particularly in forested areas where the double-bounce scattering signature is more prominent (Martinez and Le Toan, 2007; Melancon et al., 2021). To generate non-flood polygons, areas with distinct scattering characteristics, such as dry forests, open water, urban areas, and non-forest regions, were analyzed. Dry forests exhibit strong volume scattering due to canopy interactions, along with moderate peaks in single and double-bounce scattering, thereby producing a green hue. Open water shows extremely low backscatter across all scattering types, often approaching zero in cases of specular reflection; this distinguishes it from the other land covers with a black hue. Urban areas are characterized by high double-bounce scattering from building reflections, which impart them with a distinct hue. Non-forest regions, including grasslands and barren land, typically display low volume scattering and minimal single scattering, which creates a blue hue (Melancon et al., 2021).

We selected about 0.25% of the pixels in the UAVSAR image to train and test the CNN model, based on recommendations by Colditz (2015),

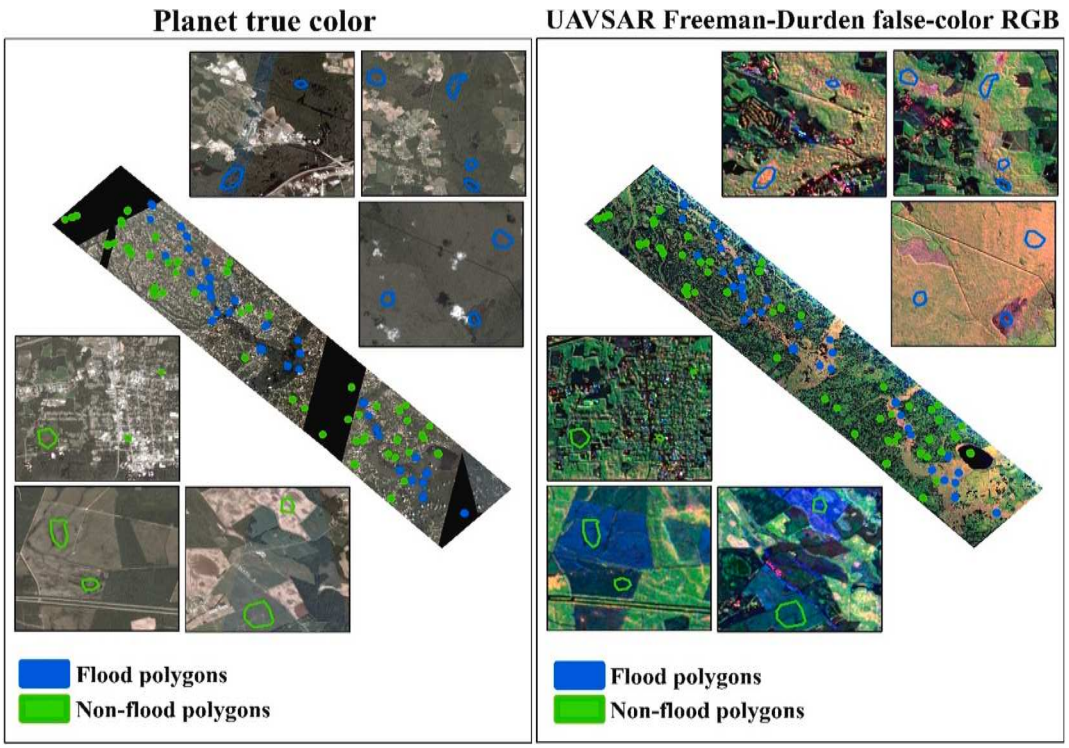

Fig. 4. Examples of manually selected flood and non-flood polygons based on Planet true-color and UAVSAR false-color RGB images.

Thanh Noi and Kappas (2018), and Melancon et al. (2021). A total of 222,175 pixels were generated to model flood, comprising 115,065 non-flood and 107,110 flood pixels. The entire set of pixels was split into training and testing sets, with 80% (177,740 pixels) allocated for training and 20% (44,435 pixels) for testing, following the protocol used by Elkhrachy (2022).

Fig. 4 shows samples of the flood and non-flood polygons over the study area on September 18, 2018, based on the Planet true-color and UAVSAR false-color RGB images.

We also considered a portion of Texas affected by Hurricane Harvey to evaluate the generalizability of the DT-RFE–CNN model. Only test data were prepared for this region, which were generated through a process similar to that described earlier. Specifically, for Hurricane Harvey, testing samples comprising flood and non-flood polygons were digitized from high-resolution imagery—including a UAVSAR false-color RGB composite, Planet true-color images, and NOAA true-color images acquired during Hurricane Harvey (National Oceanic and Atmospheric Administration, 2017). The selected polygons comprised 29,232 flood and 30,316 non-flood pixels on August 31, 2017, and 22,272 flood and 24,884 non-flood pixels on September 2, 2017.

3.6. CNN

A CNN is a deep learning architecture designed for handling structured, grid-like data, such as images. It employs convolutional layers to automatically identify and extract key features from input images by applying different filters, thus generating feature maps (LeCun et al., 2015). These feature maps are then downsampled using pooling layers to reduce computational complexity and highlight important features. Finally, fully connected layers are employed to classify the images based on the features extracted by the preceding layers (Yamashita et al., 2018).

Each convolutional layer includes a rectified linear unit (ReLU) activation function to effectively capture nonlinear patterns between the input and output variables. Let Z^j represent the feature map in the j-th layer. The output for the subsequent ($j+1$-th) layer can be expressed as follows:

$$Z^{j+1} = f\left(W^{j+1} \bullet Z^j + b^{j+1}\right) \tag{3}$$

where W^{j+1} and b^{j+1} represent the weight matrix and bias vector, respectively, which are used to relate the feature maps of the j-th and $j+1$-th layers to each other; f denotes the ReLU activation function. After passing through the convolutional layer, the feature map from the final pooling layer is flattened, which gradually reduces the feature dimensions to create a compact feature representation before the output layer (Byun et al., 2023).

As the dataset used in this work included manually digitized polygons, and as pixel-level labels were not available for the study area, we adopted a CNN-2D model adapted for tabular-format data to efficiently utilize the available labeled samples. Fig. 5 shows the structure of the CNN model developed for inundation mapping. The architecture includes multiple layers specifically designed to distinguish between flooded and non-flooded areas. The model comprises two convolutional layers, two pooling layers, two fully connected layers, and one output layer. The final layer is crucial for accurately identifying flooded areas. Table 2 presents the detailed specifications of the CNN model.

3.7. Evaluation metrics

We evaluated the proposed model's performance in detecting flooded areas based on five indicators: accuracy, precision, recall, F1 score, and IoU. Accuracy represents the proportion of correctly predicted pixels among all the pixels. Precision denotes the proportion of correct positive predictions, while recall reflects the proportion of actual positive cases that were correctly identified. F1 score is the harmonic mean of precision and recall, offering a balanced measure of these two metrics; a higher F1 score indicates a better balance between precision and recall.

IoU is used to evaluate the overlap between the predicted area and the ground-truth area. It is calculated as the intersection of the predicted and actual regions divided by the area of their union. IoU ranges from

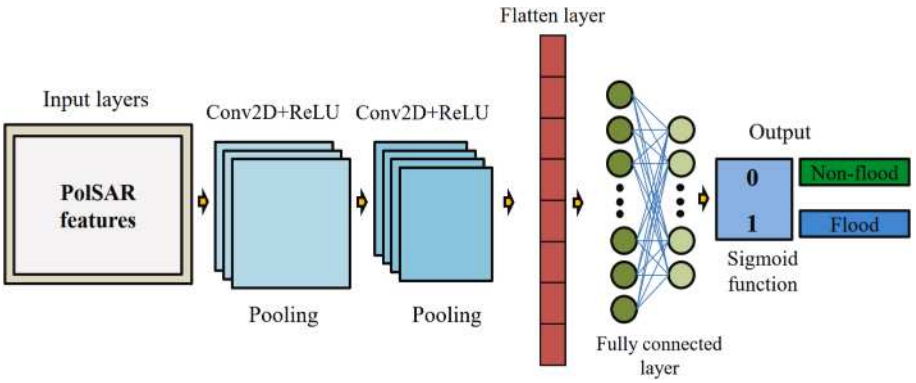

Fig. 5. Structure of the CNN model for flood mapping.

Table 2
Specifications of the CNN model (*N*: number of input features).

Layer	Shape	Output size
Input	(*N*, 1, 32)	–
Conv2D	(3 × 3, 32 filters)	(*N*, 1, 32)
BatchNorm	–	(*N*, 1, 32)
MaxPooling2D	(2 × 2)	(*N*/2, 1, 32)
Dropout	(Rate: 0.25)	(*N*/2, 1, 32)
Conv2D	(3 × 3, 64 filters)	(*N*/2, 1, 64)
BatchNorm	–	(*N*/2, 1, 64)
MaxPooling2D	(2 × 2)	(*N*/4, 1, 64)
Dropout	(Rate: 0.25)	(*N*/4, 1, 64)
Flatten	–	*N*/4 × 64
Dense	(128 units)	128
Dropout	(Rate: 0.5)	128
Dense	(1 unit)	1

0 to 1, with 1 representing a perfect match between the prediction and the ground truth and 0 indicating no overlap. Higher IoU values indicate better model accuracy in detecting and delineating the flooded area. The equations for calculating the aforementioned indicators are as follows:

$$\text{Accuracy} = \frac{TP + TN}{TP + TN + FP + FN} \tag{4}$$

$$\text{Precision} = \frac{TP}{TP + FP} \tag{5}$$

$$\text{Recall} = \frac{TP}{TP + FN} \tag{6}$$

$$\text{F1} = \frac{2 \times \text{Precision} \times \text{Recall}}{\text{Precision} + \text{Recall}} \tag{7}$$

$$\text{IoU} = \frac{TP}{TP + FN + FP} \tag{8}$$

where *TP* refers to true positive (the number of ground-truth flood pixels correctly predicted by the model), *FP* represents false positive (the number of ground-truth non-flood pixels incorrectly classified by the model as flood pixels), *FN* indicates false negative (the number of ground-truth flood pixels mistakenly predicted by the model as non-flood pixels), and *TN* denotes true negative (the number of ground-truth non-flood pixels correctly predicted by the model).

3.8. Different approaches for flood mapping

In this study, two additional approaches were considered for comparison with the DT-RFE–CNN model. First, we applied the Otsu method (Otsu, 1979), a classical thresholding technique. Second, we replaced the CNN with a more recent ML model, i.e., the feature tokenizer and transformer (FT-Transformer) model (Gorishniy et al., 2023), a state-of-the-art model designed for tabular data. For this model, the input features selected via DT-RFE were used.

3.8.1. Ostu thresholding method

Thresholding is a classical approach for detecting flooded areas using SAR data (Cao et al., 2019). The thresholds of backscatter data between flooded and non-flooded areas are typically determined by trial and error (Rahman and Thakur, 2018), which is subjective and time-consuming (Tong et al., 2018). To address these limitations and enhance accuracy, automated binary thresholding methods (Moharrami et al., 2021) have been developed for image segmentation and pattern recognition (Sezgin and Sankur, 2004; Wunnava et al., 2020).

Among automated thresholding methods, the Otsu method is regarded as one of the most effective (Moharrami et al., 2021) for flood representation using SAR images (Du et al., 2014; Li et al., 2014; Pan et al., 2020; Zhang et al., 2020). This method iteratively examines all possible values to determine the optimal threshold. The objective is to maximize the inter-class variance between two segments and minimize the intra-class variance (Otsu, 1979).

In the Otsu method, pixels are divided into two classes: Class 1 (C1) in the range $[a, t]$ and Class 2 (C2) in the range $[t, b]$, where t is the threshold. The optimal threshold is determined as the value that maximizes the inter-class variance between C1 (flooded areas) and C2 (non-flooded areas) as

$$\sigma^2 = P_{c1} \bullet (\mu_{c1} - \mu)^2 + P_{c2} \bullet (\mu_{c2} - \mu)^2 \tag{9}$$

where σ^2 represents the inter-class variance between C1 and C2. P_{c1} and P_{c2} are the probabilities of pixel distributions in C1 and C2, respectively. μ_{c1} and μ_{c2} are the mean values of the pixels in C1 and C2, respectively, and μ is the mean value of the indexed image. Following Dang et al. (2024), we used VV polarization, which is known to be the most effective for distinguishing flooded areas among various types of backscattering.

3.8.2. FT-transformer

FT-Transformer represents a modified architecture of the Transformer model (Vaswani et al., 2017), designed to handle both continuous and categorical features in tabular or time-series data (Gorishniy et al., 2021). The concept is to convert all continuous and categorical features into token embeddings and then learn the relationships among these features using the self-attention mechanism of the Transformer (Gorishniy et al., 2021).

Fig. 6 illustrates the architecture of FT-Transformer. The feature tokenizer module encodes numerical and categorical features into tokens that can be input to the Transformer. This structure is specifically designed to adapt tabular data for Transformer-based models. Subsequently, the Transformer module captures the inter-feature dependencies through feature-wise self-attention. Lastly, a special

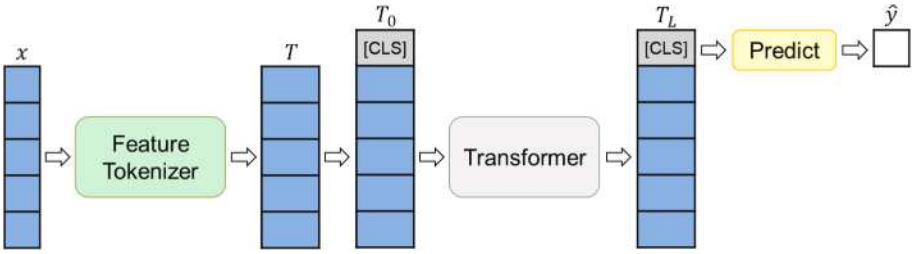

Fig. 6. FT-Transformer architecture.

classification token (CLS) integrates information from all feature embeddings to generate the final prediction. Details of the FT-Transformer model can be found in the work of Gorishniy et al. (2021).

4. Results and discussions

4.1. Flood mapping over Lumber flight path in North Carolina

4.1.1. Multicollinearity analysis

To select independent PolSAR features from the pool of 100 generated features, we conducted a multicollinearity analysis based on VIF. Following a previous method (James et al., 2023; Menard, 2001; Vittinghoff et al., 2012), 49 features with a VIF of less than 10 were selected for flood mapping (Table 3).

4.1.2. Feature selection

Table 4 shows the importance of the features obtained using DT-RFE. The Alpha_s feature from the Touzi method demonstrated overwhelmingly high importance. This feature measures the magnitude of symmetric scattering, ranging from 0° to 90°, where values near 0° correspond to surface scattering, those around 45° indicate volume scattering, and those near 90° represent double-bounce scattering (Dabboor and Shokr, 2023). Moreover, the top 7 and 10 features respectively accounted for approximately 85% and 90% of the total importance, which indicates that the importance was heavily concentrated on only a few features. However, drawing definitive conclusions on the number of features needed to maximize the CNN model's accuracy is difficult.

Table 3
PolSAR features selected through VIF-based multicollinearity analysis.

PolSAR feature	VIF	PolSAR feature	VIF
AGH_Alphap_SM1	4.44	NEU_Delta_pha	3.02
AGH_Orientation_max_SM2	1.39	NEU_Tau	5.28
AGH_Orientation_max_mean	1.69	SIN4_Hlx	< 0.01
AGH_Phip_SM1	1.46	7SD_CD	3.22
AGH_Phip_SM2	2.05	7SD_Hlx	3.70
AGH_Phip_SM3	2.24	7SD_MD	5.39
AGH_Tawp_SM1	3.43	7SD_OD	2.96
AGH_Tawp_SM2	2.51	7SD_Vol	4.59
AGH_Tawp_SM3	1.76	6SD_CD	4.78
AN4_Vol	9.99	6SD_OD	4.40
ANNED_Odd	3.52	6SD_Vol	7.77
BF4_Vol	2.45	TSVM_Alpha_s	4.23
HAA_Alpha	2.43	TSVM_Alpha_s2	3.37
HAA_Anisotropy	2.26	TSVM_Alpha_s3	1.44
HAA_Beta	3.14	TSVM_Phi_s	2.34
HAA_Delta	1.48	TSVM_Phi_s2	2.85
HAA_Entropy	7.81	TSVM_Phi_s3	1.40
HAA_Gamma	1.94	TSVM_Psi1	1.73
KRO_Kd	1.22	TSVM_Psi2	1.65
KRO_Kh	1.07	TSVM_Psi3	2.21
KRO_Ks	1.00	TSVM_Tau_m1	1.32
KRO_Teta	1.16	TSVM_Tau_m2	1.42
MCSM_Hlx	< 0.01	TSVM_Tau_m3	1.27
MCSM_Vol	< 0.01	Y4O_Hlx	4.94
MCSM_Wire	8.53		

4.1.3. Model evaluation

Table 5 summarizes the DT-RFE–CNN model's performance in inundation mapping for September 18, 2018, using different numbers of the most important features listed in Table 4. For example, the first and second rows in Table 5 present the outcomes of utilizing only the most important PolSAR feature (i.e., TSVM_Alpha_s) and the top five features (i.e., TSVM_Alpha_s, ANNED_Odd, 7SD_MD, HAA_Anisotropy, and AN4_Vol), respectively. When utilizing only the most important feature, the model achieved accuracy, precision, recall, F1 score, and IoU values of 0.8909, 0.9155, 0.8527, 0.8830, and 0.7905 for the training phase and 0.8903, 0.9113, 0.8539, 0.8816, and 0.7884 for the testing phase, respectively. Expectedly, utilizing more PolSAR features improves the model's performance, allowing it to map flooded areas more accurately. The model performed the best when using the top 40 features (among the 49 shown in Table 4), demonstrating strong results across all metrics. On the training data, the model achieved an accuracy of 0.9750, a precision of 0.9866, a recall of 0.9613, an F1 score of 0.9738, and an IoU of 0.9489; on the testing data, it maintained robust performance, with an accuracy of 0.9724, a precision of 0.9823, a recall of 0.9596, an F1 score of 0.9708, and an IoU of 0.9433. The best-performing DT-RFE–CNN model showed a balance between precision and recall. This balance means that the model could accurately predict both positive and negative cases while effectively limiting false positives and false negatives, which enables more reliable decision-making (Saito and Rehmsmeier, 2015). Additionally, similar precision and recall values tend to maximize the F1 score (the harmonic average of these two metrics), indicating strong overall performance, especially on imbalanced datasets. This results in a more trustworthy model, capable of consistent performance across various scenarios.

For a computer equipped with an AMD Ryzen Threadripper PRO 7995WX 96-core CPU, the times required to train and test the DT-RFE–CNN model with the top 1, 40, and 49 features were about 29, 46, and 53 min, respectively.

We examined how the number of features affects both accuracy and the F1 score because accuracy measures the overall proportion of correct predictions across all classes while F1 score combines precision and recall into a single, balanced performance metric. Fig. 7 illustrates the variation in these metrics with the number of PolSAR features during the training and testing phases. A sharp rise in the metrics is observed when the number of features increases from 1 to 10, but the behavior becomes asymptotic with the addition of further features. This indicates that most of the information required for mapping inundated areas exists within the top 10 features and that using more features does not improve the results significantly. The features generated through Touzi decomposition (Touzi, 2007) account for four of the top 10 features shown in Table 4. This highlights the significance of understanding scattering characteristics through an eigenvector analysis technique, such as Touzi decomposition.

The evaluation results show that the DT-RFE–CNN model achieved the highest accuracy (0.9751) and F1 score (0.9738) during the training stage when utilizing the top 40 PolSAR features. With the same features in the testing stage, the model again achieved the highest accuracy (0.9724) and F1 score (0.9708). Overall, three conclusions can be drawn from the results shown in Table 5 and Fig. 7: (1) using more than 10

Table 4
Feature importance estimated using DT-RFE.

Feature	Importance	Feature	Importance
TSVM_Alpha_s	0.6378	AGH_Alphap_SM1	0.0027
ANNED_Odd	0.0555	AGH_Tawp_SM1	0.0026
7SD_MD	0.0496	6SD_Vol	0.0026
HAA_Anisotropy	0.0301	TSVM_Psi3	0.0026
AN4_Vol	0.0286	6SD_CD	0.0025
MCSM_Wire	0.0263	TSVM_Tau_m2	0.0025
TSVM_Alpha_s2	0.0190	TSVM_Psi2	0.0024
TSVM_Psi1	0.0150	AGH_Tawp_SM3	0.0024
HAA_Entropy	0.0148	TSVM_Phi_s3	0.0023
TSVM_Phi_s	0.0148	AGH_Tawp_SM2	0.0022
BF4_Vol	0.0107	TSVM_Phi_s2	0.0021
HAA_Alpha	0.0073	HAA_Beta	0.0019
NEU_Tau	0.0062	7SD_CD	0.0017
7SD_Hlx	0.0060	TSVM_Alpha_s3	0.0015
NEU_Delta_pha	0.0050	AGH_Orientation_max_SM2	0.0015
HAA_Gamma	0.0046	6SD_OD	0.0014
Y4O_Hlx	0.0045	KRO_Kd	0.0014
AGH_Phip_SM2	0.0037	KRO_Teta	0.0011
HAA_Delta	0.0032	KRO_Ks	0.0010
AGH_Phip_SM1	0.0030	7SD_OD	0.0010
AGH_Orientation_max_mean	0.0029	KRO_Kh	0.0007
AGH_Phip_SM3	0.0029	MCSM_Hlx	< 0.0001
TSVM_Tau_m3	0.0028	MCSM_Vol	< 0.0001
TSVM_Tau_m1	0.0028	SIN4_Hlx	< 0.0001
7SD_Vol	0.0028		

Table 5
Performance metrics of the DT-RFE–CNN model for flood mapping with different numbers of PolSAR features during training and testing phases.

Number of top features utilized	Stage	Accuracy	Precision	Recall	F1 score	IoU
1	Training	0.8909	0.9155	0.8527	0.8830	0.7905
	Testing	0.8903	0.9113	0.8539	0.8816	0.7884
5	Training	0.9541	0.9722	0.9315	0.9515	0.9074
	Testing	0.9563	0.9732	0.9344	0.9534	0.9109
10	Training	0.9685	0.9822	0.9520	0.9669	0.9358
	Testing	0.9695	0.9812	0.9545	0.9677	0.9373
15	Training	0.9711	0.9841	0.9555	0.9696	0.9410
	Testing	0.9710	0.9824	0.9566	0.9693	0.9405
20	Training	0.9728	0.9871	0.9563	0.9714	0.9445
	Testing	0.9719	0.9839	0.9569	0.9702	0.9422
25	Training	0.9716	0.9908	0.9501	0.9700	0.9418
	Testing	0.9709	0.9889	0.9500	0.9690	0.9399
30	Training	0.9739	0.9842	0.9614	0.9727	0.9468
	Testing	0.9723	0.9808	0.9610	0.9706	0.9432
35	Training	0.9747	0.9879	0.9594	0.9734	0.9482
	Testing	0.9722	0.9841	0.9574	0.9705	0.9427
40	Training	0.9751	0.9866	0.9613	0.9738	0.9489
	Testing	0.9724	0.9823	0.9596	0.9708	0.9433
45	Training	0.9750	0.9842	0.9637	0.9737	0.9490
	Testing	0.9716	0.9799	0.9604	0.9700	0.9418
49	Training	0.9748	0.9842	0.9634	0.9737	0.9487
	Testing	0.9720	0.9798	0.9613	0.9705	0.9426

PolSAR features does not improve model performance significantly; (2) most of the information required for flood mapping is concentrated within the top 10 features; and (3) the model performs best in terms of both accuracy and F1 score across the training and testing phases when using the top 40 PolSAR features.

The confusion matrix in Fig. 8 illustrates the performance of the DT-RFE–CNN model with the top 40 features. This matrix visualizes the performance of the model based on the number of correct and incorrect predictions (Sokolova and Lapalme, 2009). As seen in Fig. 8, among the 177,740 training samples, 97.50% were correctly classified (TP: 46.43%, TN: 51.07%) while only 2.50% were misclassified (FP: 0.63%, FN: 1.87%). For the testing dataset comprising 44,435 samples, 97.24% were correctly classified (TP: 45.93%, TN: 51.31%) while 2.76% were misclassified (FP: 0.83%, FN: 1.94%). The high percentage of correctly classified flood and non-flood pixels on both the training and testing data demonstrates that the developed hybrid model can be reliably used by decision-makers to improve flood management strategies and disaster response planning.

4.1.4. *Mapping of flooded regions*

Based on the model evaluation results, the flood map for the Lumber flight path on September 18, 2018, was generated by providing the DT-RFE–CNN model with the top 40 PolSAR features. As explained earlier, the features were used as the inputs while samples of flood and non-flood pixels across the Lumber flight path on September 18, 2018, were used as the outputs to train and test the model. The flood map generated for the entire Lumber flight path is depicted in Fig. 9, where the blue and green portions represent the flooded and non-flooded regions, respectively. Expectedly, regions along the Lumber River and those with low elevations (with reference to Fig. 1) were classified as flooded, whereas areas with higher elevations were categorized as non-flooded. Overall, a consistency was observed between the flood and elevation maps, which indicates that the DT-RFE–CNN model can reliably identify flooded regions.

To further evaluate the robustness of the DT-RFE–CNN model, it was used to estimate the flood maps over the Lumber flight path on September 19, 20, 22, and 23, 2018 (Fig. 10). As explained in Section 3.5, polygons delineating flooded and non-flooded regions were created for these days based on the Planet true-color and UAVSAR false-color RGB composite images. These polygons comprise 22,149 flood and 22,234 non-flood pixels for September 19; 22,255 flood and 22,367 non-flood pixels for September 20; 22,392 flood and 22,500 non-flood pixels for September 22; and 22,491 flood and 22,360 non-flood pixels for September 23 and were used to evaluate the flood maps generated for these days.

Table 6 summarizes the performance metrics of the DT-RFE–CNN model for the aforementioned dates. The model performed well, exhibiting accuracy, precision, recall, F1 Score, and IoU values of 0.9123–0.9552, 0.8643–0.9493, 0.9152–0.9874, 0.9123–0.9556, and 0.8388–0.9150, respectively. On average, the model achieved an accuracy of 0.9304, a precision of 0.9089, a recall of 0.9584, an F1 Score of 0.9324, and an IoU of 0.8738 for September 19, 20, 22, and 23, respectively. These results underscore the model's accuracy in

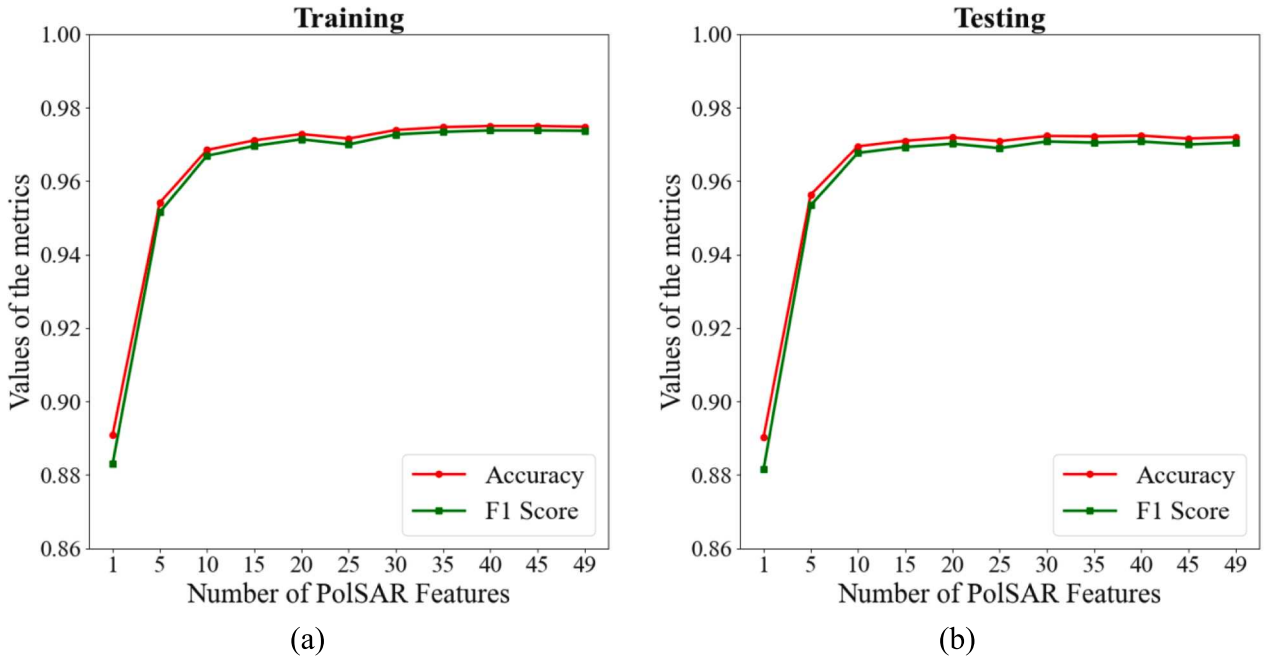

Fig. 7. Variation in accuracy and F1 score of the DT-RFE–CNN model with number of PolSAR features during training and testing stages.

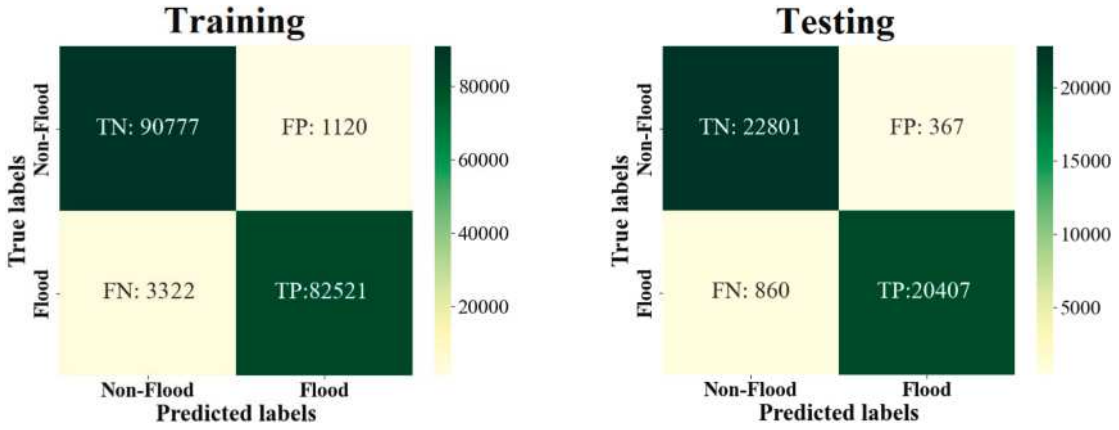

Fig. 8. Confusion matrices of the DT-RFE–CNN model with top 40 features during training and testing stages.

predicting flood maps across different temporal instances.

Notably, the recall was higher than the precision, which indicates that the model prioritizes capturing as many true positives as possible, even if it increases the false positive rate (Saito and Rehmsmeier, 2015). Thus, the model focuses more on minimizing missed positive cases, which can be beneficial in scenarios where detecting every positive instance is crucial, even at the expense of slightly lower prediction accuracy. In summary, the proposed model favors completeness over precision to ensure fewer missed positives with the trade-off being potentially higher false positive rates.

Table 7 presents the areas (km^2) of flooded and non-flooded regions estimated by the DT-RFE–CNN model for different days. Fig. 11 shows the daily domain-average precipitation (mm) and flooded area (km^2). The 1-km daily precipitation data for the study domain were obtained from the Daymet product (Thornton et al., 2022). The rainfall intensity associated with Hurricane Florence was high on September 14–16 but significantly decreased on September 17 and 18. Owing to the intense rainfall, the flooding persisted for an extended duration. As anticipated, the maximum flooded area (2,692.1 km^2) was observed on September 18 (shortly after intense rainfall), and its value decreased to 2,583.8 and 2,378.5 km^2 on September 19 and 20, respectively (Table 7 and Fig. 11).

Although no rainfall was recorded over the study domain on September 22 and 23, the inundated area increased slightly on these dates. This is likely because of the lower elevation of the study area (Fig. 12): Flood water flowing downstream from the upper basin caused repeated inundation in many locations. For instance, Fig. 13 shows the changes in the water level at two USGS gauges within the study area in response to Hurricane Florence (https://waterdata.usgs.gov/). The drainage areas of the Lumber River near Maxton gauge (ID: 02133624) and at Lumberton gauge (ID: 02134170) are 946 km^2 and 1,834 km^2, respectively. At the Lumberton gauge, which is located downstream, the initial peak in water level on September 18 was attributable to intense rainfall close to the gauge, while the secondary peak on September 21 was caused by water moving downstream along the Lumber River. In addition to the lag between rainfall at higher elevations and its resulting runoff downstream, the slow movement of Florence caused prolonged rainfall in specific areas, leading to a rise in groundwater levels and reduced drainage (Humphrey Jr. et al., 2021; Ross, 2018). Hence, certain areas experienced prolonged or recurring flooding. These findings suggest that comprehensive flood management, including both

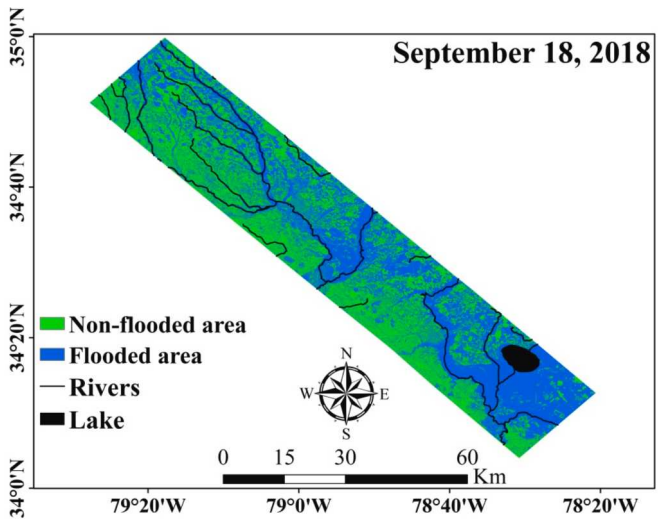

Fig. 9. Flood map for Lumber flight path on September 18, 2018, generated by the DT-RFE–CNN model using top 40 PolSAR features.

rapid response and systemic improvements to prevent recurrence, is necessary to mitigate flood damage during large-scale rainfall events.

4.2. Comparison between flood mapping using PolSAR data and PolSAR features

We established a CNN model that utilizes PolSAR data and compared its performance with that of our innovative hybrid model. For this purpose, PolSAR data comprising six polarization combinations (i.e., $S_{HH}S^*_{HH}$, $S_{HV}S^*_{HV}$, $S_{VV}S^*_{VV}$, $S_{HH}S^*_{HV}$, $S_{HH}S^*_{VV}$, and $S_{HV}S^*_{VV}$) were employed as the input for the CNN model. The flood and non-flood polygons specified in Section 3.5 (i.e., 115,065 non-flood and 107,110 flood pixels) were also used as the output for this model. The dataset was split into training and testing sets, with 80% (177,740 pixels) allocated for training and 20% (44,435 pixels) reserved for testing. The training and testing pixels were consistent with those used for flood mapping based on PolSAR features.

The aforementioned CNN model was used to generate the flood map over the Lumber flight path for September 18, 2018. Fig. 14 displays the confusion matrix of this model for the training and testing phases, showing that among the 177,740 training samples, 89.68% were

Table 6
Performance metrics of the DT-RFE–CNN model for different days.

Date	Accuracy	Precision	Recall	F1 score	IoU
September 19, 2018	0.9381	0.9124	0.9691	0.9399	0.8866
September 20, 2018	0.9123	0.9095	0.9152	0.9123	0.8388
September 22, 2018	0.9552	0.9493	0.9620	0.9556	0.9150
September 23, 2018	0.9159	0.8643	0.9874	0.9217	0.8548

Table 7
Areas (km^2) of flooded and non-flooded regions predicted by the DT-RFE–CNN model for different days.

Dates	Flooded area		Non-flooded area		Total area	
	(km^2)	(%)	(km^2)	(%)	(km^2)	(%)
September 18, 2018	2,692.1	56.5	2,076.4	43.5	4,768.5	100
September 19, 2018	2,583.8	54.2	2,184.7	45.8		
September 20, 2018	2,378.5	49.9	2,390.0	50.1		
September 22, 2018	2,456.8	51.5	2,311.7	48.5		
September 23, 2018	2,472.5	51.9	2,296.0	48.1		

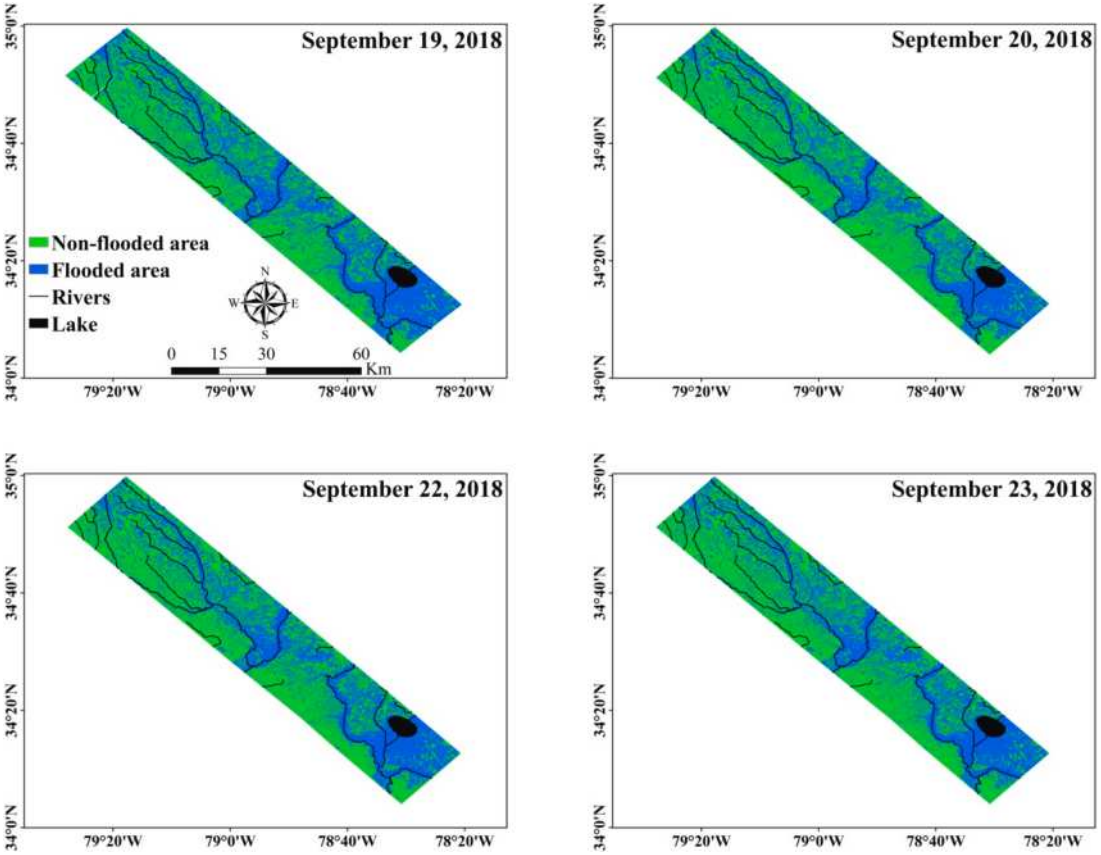

Fig. 10. Flood maps for Lumber flight path on different days predicted by the DT-RFE–CNN model using top 40 PolSAR features.

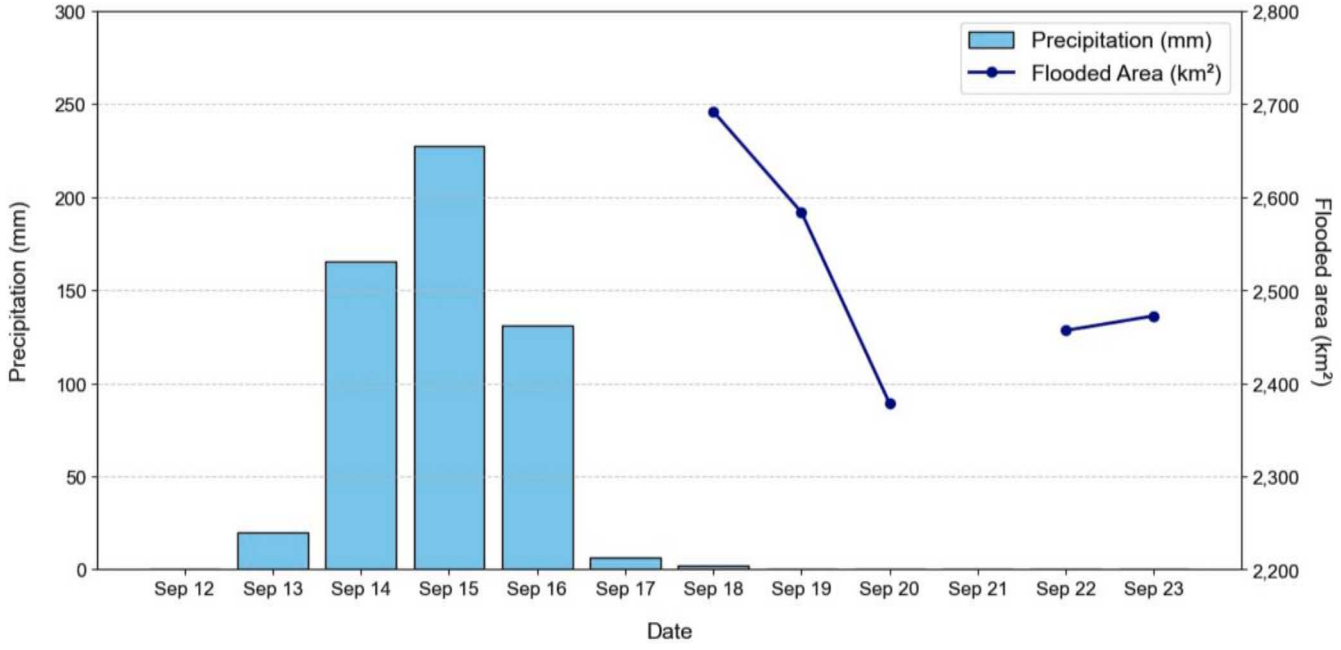

Fig. 11. Time series of domain-averaged precipitation (mm) and area (km^2) of the flooded regions.

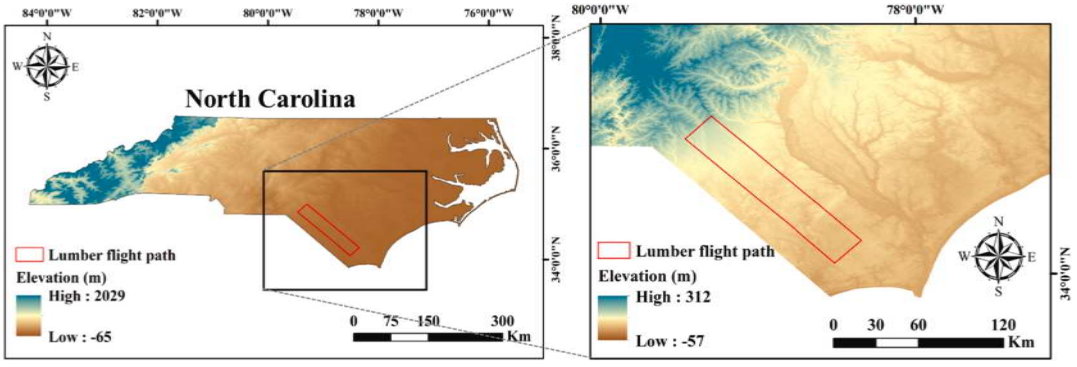

Fig. 12. Elevation map of the Lumber flight path and surrounding regions.

correctly classified (TP: 42.33%, TN: 47.35%) while 10.32% were misclassified (FP: 4.35%, FN: 5.97%); these values are worse than the corresponding results for the DT-RFE–CNN model (97.50% correctly classified and 2.50% incorrectly classified pixels in the training step). On the testing dataset, which comprised 44,435 samples, 89.89% were correctly classified (TP: 42.17% and TN: 47.72%) while 10.11% were misclassified (FP: 4.42% and FN: 5.69%) by the CNN model based on PolSAR data; these values are again worse than the corresponding results for the DT-RFE–CNN model (97.24% correctly classified and 2.76% misclassified pixels). Thus, the DT-RFE–CNN model based on PolSAR features clearly outperformed the CNN model based on PolSAR data.

Table 8 summarizes the performance metrics of the CNN model based on PolSAR data during the training and testing stages; for comparison, the corresponding metrics of the DT-RFE–CNN are also shown in parenthesis. The comparison highlights the improvement in the flood mapping efficacy achieved when using PolSAR features rather than PolSAR data. The DT-RFE–CNN model, which utilizes PolSAR features, demonstrated superior performance across all metrics in both the training and testing stages. Referring to the testing stage, the improvement in accuracy and precision achieved by the DT-RFE–CNN model underlines its stronger ability to correctly identify flood areas. Similarly, the better recall value highlights the model's capacity to detect more flood instances. The improvement in F1 score, which represents a balance between precision and recall, reflects an enhancement in overall performance. Most notably, the improvement in IoU underscores the greater overlap between the predicted and actual flood areas. These results strongly suggest that the use of PolSAR features in the DT-RFE–CNN model enhances its flood-mapping capabilities, providing more accurate and reliable predictions than those achievable using PolSAR data.

4.3. Comparison of flood mappings from different approaches

The Otsu method was used to generate the flood map over the Lumber flight path for September 19, 20, 22, and 23, 2018, and its results were compared with those of DT-RFE–CNN. To this end, backscatter intensity information from the VV polarization channel was extracted from the covariance matrix. A 3 × 3 sliding-window boxcar filter was applied to reduce speckle noise, and the resulting image was subsequently converted to the decibel (dB) scale. The Otsu method was then applied to the backscatter data for each date (September 19, 20, 22, and 23, 2018) to determine the threshold value, classifying pixels below the threshold as C1 (flooded) and those above the threshold as C2 (non-flooded).

Fig. 15 presents the thresholding results obtained using the Otsu method, along with the corresponding histogram of VV backscatter

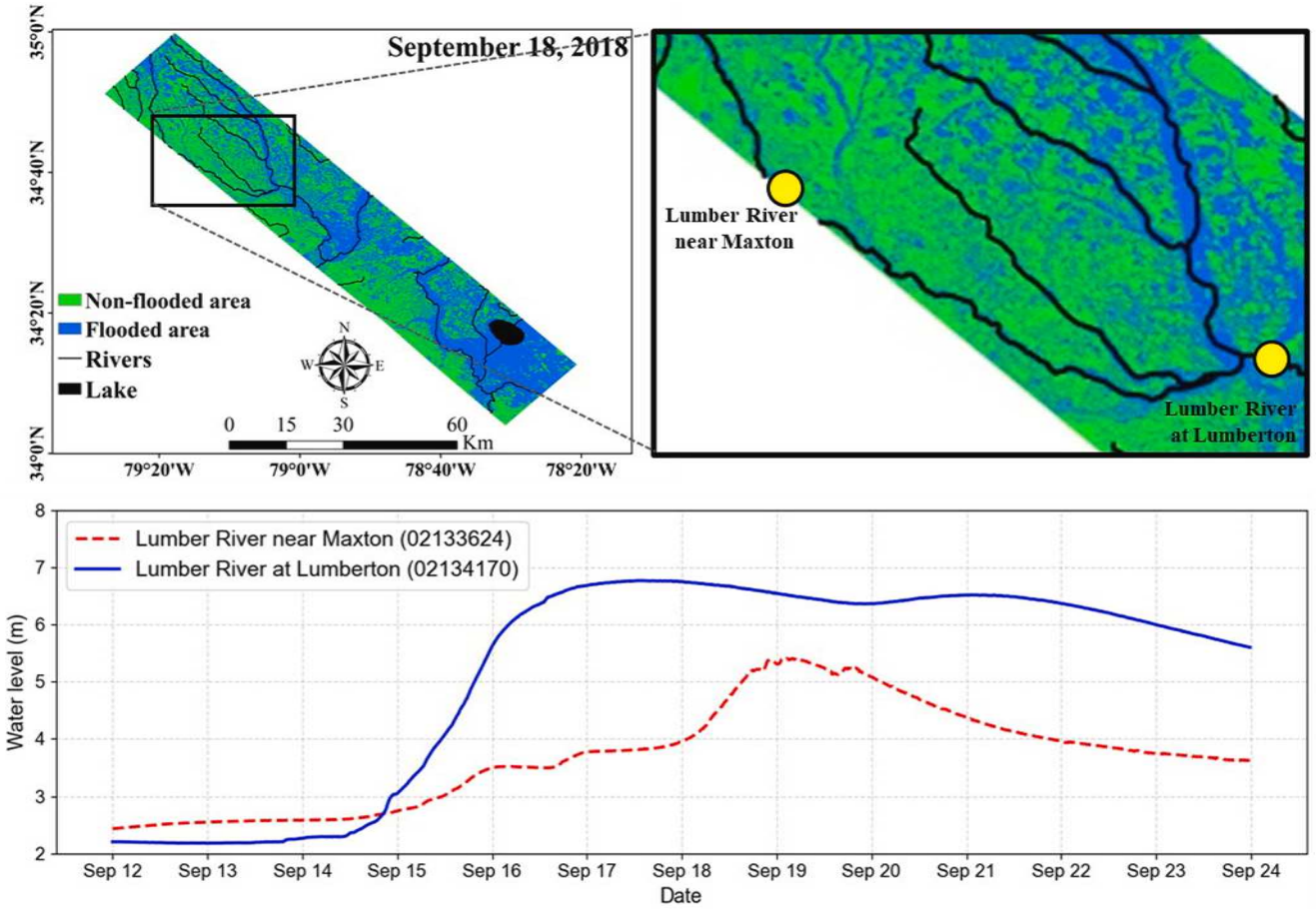

Fig. 13. (top row) Locations of the two USGS gauging stations in the Lumber flight path, and (bottom row) changes in water level at the two USGS stations from September 12 to 24, 2018.

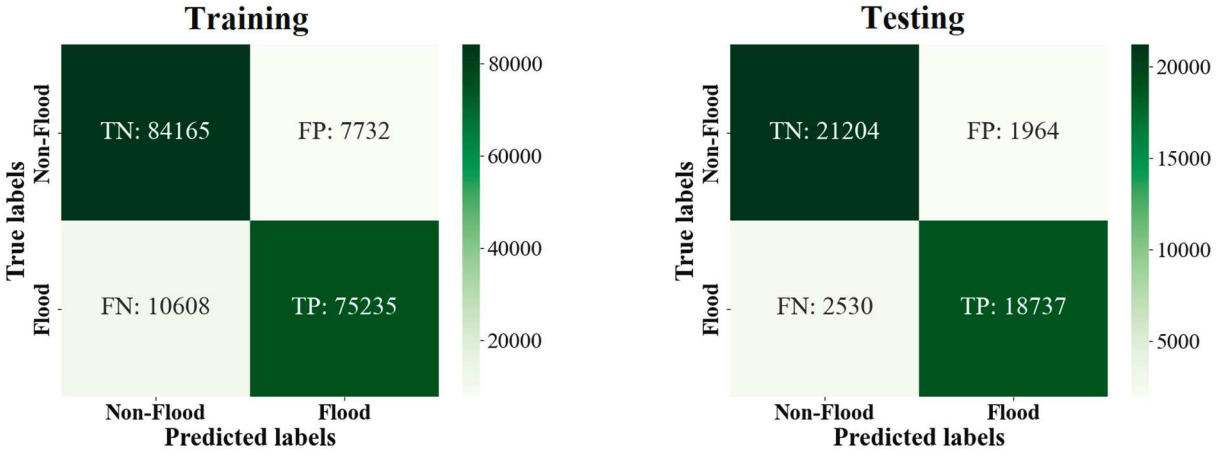

Fig. 14. Confusion matrices of the CNN model based on PolSAR data during training and testing stages.

intensity for the entire domain on different dates. The threshold values for September 19, 20, 22, and 23, 2018 were −9.49, −9.79, −9.78, and −9.96 dB, respectively, showing high consistency across the four days. Pixels with values below the threshold were classified as flooded areas, while those above were identified as non-flooded areas.

Based on the Otsu method, approximately 32.9%, 29.6%, 30.2%, and 28.7% of the study area was classified as flooded on September 19, 20, 22, and 23, 2018, respectively. The corresponding values obtained using the DT-RFE–CNN model were 54.2%, 49.9%, 51.5%, and 51.9%, significantly higher than those of the Otsu method. Table 9 presents a comparison of the results based on the validation dataset on September 19, 20, 22, and 23, 2018. The Otsu method yielded poor results, with an accuracy of 0.1791, a precision of 0.0091, a recall of 0.0057, an F1 score of 0.0069, and an IoU of 0.0035 on average across the four days.

Calm water surfaces typically appear dark in SAR imagery owing to specular reflection, as they tend to reflect radar signals away from the sensor (Tarpanelli et al., 2022; Zhao, 2022). However, when the water surface becomes rough (owing to wind, current, or rainfall), the

Table 8
Performance metrics of the CNN model based on PolSAR data during training and testing stages; corresponding results of DT-RFE–CNN model using PolSAR features are shown in parentheses for comparison.

Stage	Accuracy	Precision	Recall	F1 score	IoU
Training	0.8968 (0.9751)	0.9068 (0.9866)	0.8764 (0.9613)	0.8914 (0.9738)	0.8040 (0.9489)
Testing	0.8988 (0.9724)	0.9051 (0.9823)	0.8810 (0.9596)	0.8929 (0.9708)	0.8065 (0.9433)

backscatter increases, rendering it challenging to accurately identify flooded areas. Moreover, global thresholding approaches fail to account for variations in backscatter intensity caused by topography, sensor range, or local incidence angle (Liang and Liu, 2020). Features such as vegetation-covered flooded areas, urban shadows, or wet soil often exhibit low backscatter values, which can result in their misclassification as flooded regions (Tarpanelli et al., 2022). These observations underscore the limitations of simple intensity-based thresholding and highlight the necessity of employing PolSAR decompositions as well as metaheuristic optimization and deep-learning approaches, which can provide physically interpretable scattering components for more accurate flood mapping.

Subsequently, FT-Transformer was applied using the 40 features obtained from DT-RFE. Table 10 compares the results of the FT-Transformer and DT-RFE–CNN models. Despite using the same set of 40 PolSAR features, FT-Transformer exhibited inferior results compared with DT-RFE–CNN. In the training phase, FT-Transformer achieved accuracy, precision, recall, F1 score, and IoU values of 0.8949, 0.9204, 0.8566, 0.8873, and 0.7975, respectively, which are 8.2%, 6.7%, 10.9%, 8.6%, and 15.9% lower than those achieved by DT-RFE–CNN. Similarly, in the testing phase, FT-Transformer achieved accuracy, precision, recall, F1 score, and IoU values of 0.8952, 0.9171, 0.8586, 0.8869, and 0.7967, respectively, which are 7.9%, 6.6%, 10.1%, 8.4%, and 15.6% lower than those obtained using DT-RFE–CNN. These results demonstrate the superior performance of DT-RFE–CNN in both the training and testing phases across all evaluation metrics. Notably, the difference in IoU was the most pronounced, which highlights the stronger ability of DT-RFE–CNN to minimize misclassification and improve spatial consistency with the ground observations. This performance discrepancy can be attributed to differences in model architecture and their suitability to the underlying data structure. Flooded areas typically exhibit spatial continuity, and the relationship between neighboring pixels plays a critical role in the accurate detection of inundated regions. However, the FT-Transformer model lacks the ability to incorporate such spatial continuity (Azad et al., 2023; Chen et al., 2022), limiting its capacity to learn the overall patterns of flooded regions. These findings suggest that models capable of capturing spatial continuity, such as CNNs, are more suitable for flood detection tasks.

5. Generalizability of DT-RFE–CNN model to other regions

To evaluate the applicability of the trained DT-RFE–CNN model to other regions, we tested it over a region in Texas during Hurricane Harvey. In August 2017, Hurricane Harvey—a destructive Category 4 hurricane—struck the coasts of Texas and Louisiana, triggering catastrophic flooding and causing at least 68 direct fatalities in Texas alone. It lingered over southeastern Texas for about four days, producing record-breaking rainfall with a maximum of over 150 cm near Nederland, Texas. This unprecedented rainfall caused extreme flooding (Blake and Zelinsky, 2018).

UAVSAR collected data over the Houston area on August 31 and September 1–2, 2017, during the flooding caused by Hurricane Harvey. Fig. 16 shows the flight path (ID: brazos_14937) of UAVSAR passing through the Brazos River region, which was one of the regions affected

Table 9
Performance metrics of the Otsu method for September 19, 20, 22, and 23, 2018. Results of DT-RFE–CNN model using the best 40 features are shown in parentheses for comparison.

Date	Accuracy	Precision	Recall	F1 score	IoU
September 19, 2018	0.2187 (0.9381)	0.0073 (0.9124)	0.0042 (0.9691)	0.0053 (0.9399)	0.0027 (0.8866)
September 20, 2018	0.0571 (0.9123)	0.0034 (0.9095)	0.0031 (0.9152)	0.0032 (0.9123)	0.0016 (0.8388)
September 22, 2018	0.1803 (0.9552)	0.0170 (0.9493)	0.0112 (0.9620)	0.0135 (0.9556)	0.0068 (0.9150)
September 23, 2018	0.2602 (0.9159)	0.0085 (0.8643)	0.0041 (0.9874)	0.0055 (0.9217)	0.0028 (0.8548)

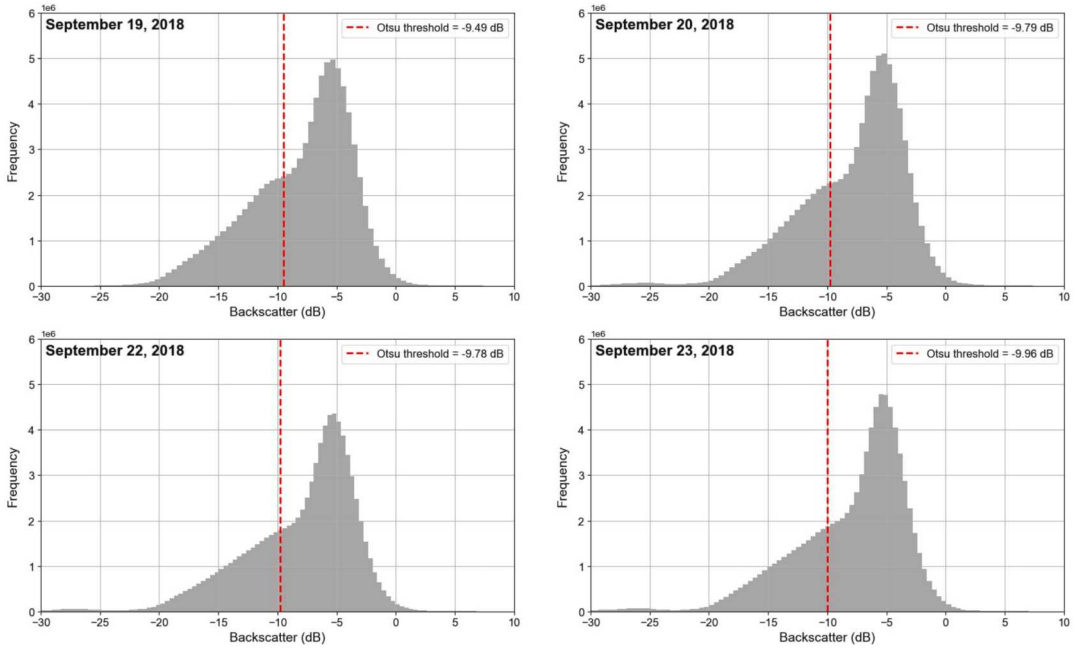

Fig. 15. Histograms of VV backscatter data and threshold values obtained using the Otsu method for September 19, 20, 22, and 23, 2018.

Table 10
Performance metrics of the FT-Transformer and the DT-RFE–CNN models during training and testing, using the same set of top 40 features.

Stage	Approach	Accuracy	Precision	Recall	F1 score	IoU
Training	FT-Transformer	0.8949	0.9204	0.8566	0.8873	0.7975
	DT-RFE–CNN	0.9751	0.9866	0.9613	0.9738	0.9489
Testing	FT-Transformer	0.8952	0.9171	0.8586	0.8869	0.7967
	DT-RFE–CNN	0.9724	0.9823	0.9596	0.9708	0.9433

by Hurricane Harvey. This area is referred to hereinafter as the "Brazos flight path." Fig. 16 illustrates the annual land use in the area for 2017, generated by the LCMS (U.S. Department of Agriculture, 2024), along with an elevation map from SRTM (NASA JPL, 2013). Many areas are rangelands, and developed regions are concentrated in the central part, with some also observed in the southern part. The elevation decreases progressively toward the coast.

The DT-RFE–CNN model trained on data over the Lumber flight path on September 18, 2018, was used to generate flood maps for the Brazos flight path. Specifically, the top 40 PolSAR features (as input) from Table 4 and the samples of flood and non-flood pixels across the Brazos flight path on September 18, 2018 (as output) were used to test the pre-trained DT-RFE–CNN model. Fig. 17 shows the predicted flood map for the Brazos flight path on August 31 and September 2, 2017; notably, the data for September 2 constitute only a subset of the swaths for August 31. Expectedly, most urban areas and low-lying regions were predicted

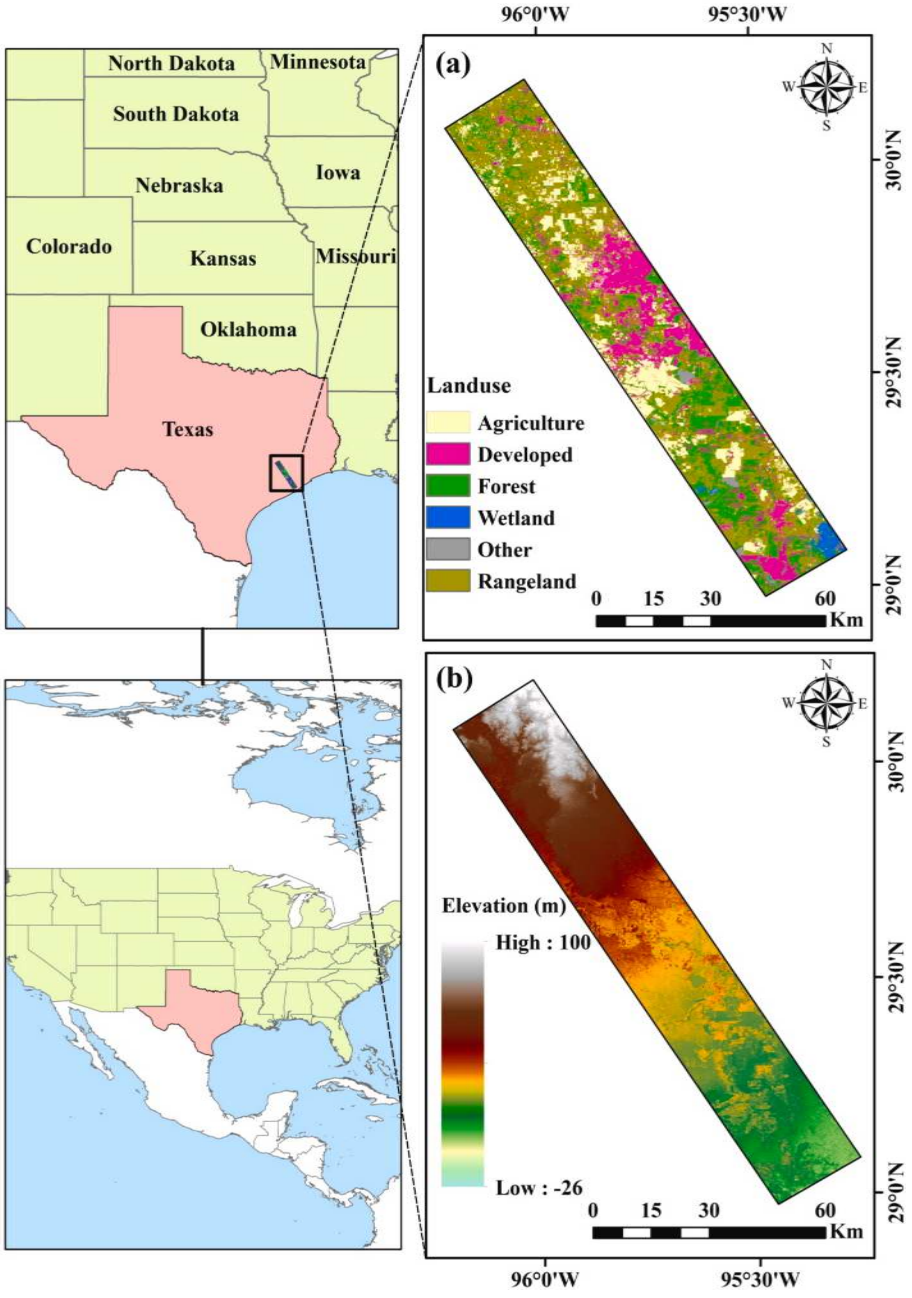

Fig. 16. Location of Brazos flight path in Texas: (a) land use and (b) elevation.

to be flooded.

Table 11 summarizes the performance metrics of the DT-RFE–CNN model when used to predict the flood map over the Brazos flight path, using the top 40 PolSAR features. For August 31, 2017, the model achieved an accuracy of 0.8279, a precision of 0.8295, and a recall of 0.8176; the F1 score and IoU were 0.8235 and 0.7000, respectively, reflecting a moderate overlap between the predicted and actual flooded areas. For September 2, 2017, the model performed better, exhibiting an accuracy of 0.8518, a precision of 0.8565, and a recall of 0.8244; its F1 score and IoU also improved to 0.8401 and 0.7244, respectively, indicating a closer agreement between the predictions and the actual observations. These test results demonstrate that the model can detect flooded areas satisfactorily, with an average accuracy, precision, recall, F1 score, and IoU of 0.8399, 0.8430, 0.8210, 0.8318, and 0.7122, respectively. Overall, the model could accurately and reliably predict flooded and non-flooded areas, showing consistently strong performance across both dates.

However, the performance metrics of the DT-RFE–CNN model for the Brazos flight path were expectedly not as strong as those for the Lumber flight path. This suggests that unless the model is tested in the same region as that on which it was trained, a certain degree of performance degradation is inevitable. This seems to be largely due to the differences in land cover between Texas and North Carolina. Texas is covered predominantly by rangeland and urban areas, whereas North Carolina is characterized by extensive forests and agricultural fields. With its widespread distribution of pine and deciduous forests, North Carolina experiences more backscattering in flood-prone areas beneath the forest canopy. This ultimately alters the characteristics of the PolSAR features, reducing the effectiveness of the DT-RFE–CNN model when trained on North Carolina and tested on a different region such as Texas.

The aforementioned discrepancy highlights the need to improve the model's robustness. This could potentially be achieved by incorporating supplementary data, such as land use, elevation, and proximity to water resources, which could improve the generalizability of the model to other regions. Additionally, further analyses involving a comparison of error rates across different land cover types, particularly in the Houston area, could be conducted to determine the land cover types contributing most to the model's inaccuracies. Such enhancements should be pursued in future work to refine the proposed DT-RFE–CNN model.

Table 11
Performance metrics of the DT-RFE–CNN model when predicting flood map over Brazos flight path.

Date	Accuracy	Precision	Recall	F1 Score	IoU
August 31, 2017	0.8279	0.8295	0.8176	0.8235	0.7000
September 2, 2017	0.8518	0.8565	0.8244	0.8401	0.7244

6. Conclusion

In this study, we introduced an innovative hybrid approach for flood detection. This approach involves extracting PolSAR features through various PolSAR decompositions, selecting independent features via multicollinearity analysis, ranking the features based on their importance using the DT-RFE method, and finally detecting flooded areas using a CNN model. The DT-RFE–CNN model was trained and tested over the Lumber flight path in North Carolina during Hurricane Florence, using sample flood and non-flood polygons over the study area obtained from visible imagery (Planet true-color and UAVSAR false-color RGB images) for September 18, 2018.

Different numbers of PolSAR features were used as input for the DT-RFE–CNN model to examine the dependence of the model's performance on the number of features. The results highlighted a considerable improvement in the evaluation metrics upon increasing the number of features from 1 to 10 but no significant enhancement with a further addition of features. The model achieved the best performance when utilizing the top 40 PolSAR features, exhibiting an accuracy of 0.9724, a precision of 0.9823, a recall of 0.9596, an F1 score of 0.9708, and an IoU of 0.9433 in the testing stage.

To further evaluate the DT-RFE–CNN model, it was tested over the Lumber flight path in North Carolina for the remaining four days of Hurricane Florence (September 19, 20, 22, and 23, 2018). The results demonstrated that the model could reliably map flooded regions even for dates on which it had not been trained. The corresponding average

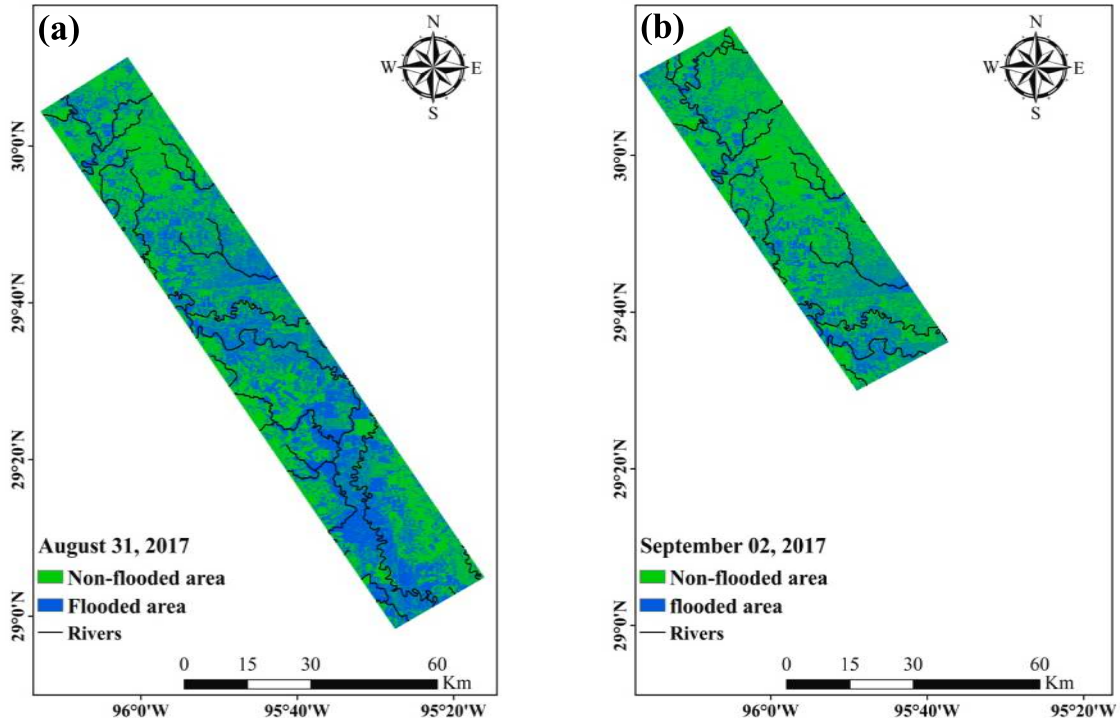

Fig. 17. Flood maps predicted by the trained DT-RFE–CNN model during Hurricane Harvey: (a) August 31, 2017, and (b) September 2, 2017.

test metrics were as follows: an accuracy of 0.9304, a precision of 0.9089, a recall of 0.9584, an F1 score of 0.9324, and an IoU of 0.8738. These results underscore the model's strong capability to accurately predict flood maps across different temporal instances.

The performance of the DT-RFE–CNN model, which uses the optimal PolSAR features, was compared with that of a CNN model utilizing PolSAR data. In the test stage, the PolSAR data–based CNN model exhibited an accuracy of 0.8988, a precision of 0.9051, a recall of 0.8810, an F1 score of 0.8929, and an IoU of 0.8065, thus being outperformed by the DT-RFE–CNN model across all metrics. These results indicate that the use of PolSAR features in the DT-RFE–CNN model substantially enhanced flood mapping accuracy and reliability compared with using PolSAR data alone. In addition, the DT-RFE–CNN model significantly outperformed both the classical Otsu thresholding method and state-of-the-art FT-Transformer model, even when using identical features (selected by DT-RFE). Additionally, the DT-RFE–CNN model's generalizability was assessed by using it to predict the flood map over the Brazos flight path in Texas for two dates during Hurricane Harvey. The test results showed that the model could detect flooded areas satisfactorily, with an accuracy of 0.8399, a precision of 0.8430, a recall of 0.8210, an F1 score of 0.8318, and an IoU of 0.7122 on average. However, as anticipated, the performance for the Brazos flight path was weaker. This seems to be largely due to the differences in land cover between Texas and North Carolina.

The proposed DT-RFE–CNN model integrates various components into a cohesive framework, achieving promising performance in flood detection. Particularly noteworthy are the novel aspects of using a wide range of decompositions to extract PolSAR features, addressing multicollinearity, and employing feature selection techniques to utilize the extracted features effectively—approaches not typically undertaken in previous research. Additionally, while the proposed model requires improvements to overcome the challenges posed by regional differences, the application of an ML model trained in one region to a completely different region without prior information still holds significant potential. The findings of this study are expected to facilitate flood monitoring and response efforts.

CRediT authorship contribution statement

Jinwook Lee: Data curation, Formal analysis, Writing – original draft, Validation. **Saeid Janizadeh:** Formal analysis, Methodology, Software, Validation. **Alexander Melancon:** Methodology, Software, Writing – review & editing. **Sayed M. Bateni:** Funding acquisition, Investigation, Supervision. **Dongkyun Kim:** Conceptualization, Writing – review & editing. **Andrew Molthan:** Project administration, Writing – review & editing. **Changhyun Jun:** Conceptualization, Writing – review & editing. **Ramin Farhadiani:** Methodology. **Saeid Homayouni:** Visualization. **Megersa Dinka:** Investigation.

Declaration of competing interest

The authors declare that they have no known competing financial interests or personal relationships that could have appeared to influence the work reported in this paper.

Acknowledgements

The authors gratefully acknowledge the support provided by the National Science Foundation (NSF) (Grant No. 2327253), the National Aeronautics and Space Administration (NASA) (Grants No. 80NSSC24K0527), the National Research Foundation (NRF) grant funded by the Korea Government (MSIT) (RS-2021-NR060085), and Korea Environment Industry & Technology Institute (KEITI) through R&D Program for Innovative Flood Protection Technologies Against Climate Crisis Program (or Project) funded by Korea Ministry of Environment (MOE) (RS-2023-00218873).

References

Adeli, S., Salehi, B., Mahdianpari, M., Quackenbush, L.J., Brisco, B., Tamiminia, H., Shaw, S., 2020. Wetland monitoring using SAR data: a meta-analysis and comprehensive review. Remote Sens. 12, 2190. https://doi.org/10.3390/rs12142190.

Adeli, S., Salehi, B., Mahdianpari, M., Quackenbush, L.J., Chapman, B., 2021. Moving toward L-band NASA-ISRO SAR mission (NISAR) dense time series: multipolarization object-based classification of wetlands using two machine learning algorithms. Earth Space Sci. 8, e2021EA001742. https://doi.org/10.1029/2021EA001742.

Aghababaee, H., Sahebi, M.R., 2018. Model-based target scattering decomposition of polarimetric SAR tomography. IEEE Trans. Geosci. Remote Sens. 56, 972–983. https://doi.org/10.1109/TGRS.2017.2757062.

Alganci, U., Sertel, E., Kaya, S., 2019. Determination of the flooded agricultural lands with Spot 6 high resolution satellite images: a case study of Menderes Plain, Turkey. In: In: 2019 8th International Conference on Agro-Geoinformatics (agro-Geoinformatics). Presented at the 2019 8th International Conference on Agro-Geoinformatics (agro-Geoinformatics), pp. 1–4. https://doi.org/10.1109/Agro-Geoinformatics.2019.8820242.

Amitrano, D., Di Martino, G., Iodice, A., Riccio, D., Ruello, G., 2018. Unsupervised rapid flood mapping using Sentinel-1 GRD SAR images. IEEE Trans. Geosci. Remote Sens. 56, 3290–3299. https://doi.org/10.1109/TGRS.2018.2797536.

An, W., Cui, Y., Yang, J., 2010. Three-component model-based decomposition for polarimetric SAR data. IEEE Trans. Geosci. Remote Sens. 48, 2732–2739. https://doi.org/10.1109/TGRS.2010.2041242.

An, W., Lin, M., 2019. A reflection symmetry approximation of multilook polarimetric SAR data and its application to Freeman–Durden decomposition. IEEE Trans. Geosci. Remote Sens. 57, 3649–3660. https://doi.org/10.1109/TGRS.2018.2886386.

An, W., Xie, C., Yuan, X., Cui, Y., Yang, J., 2011. Four-component decomposition of polarimetric SAR images with deorientation. IEEE Geosci. Remote Sens. Lett. 8, 1090–1094. https://doi.org/10.1109/LGRS.2011.2157078.

Andrew, O., Apan, A., Paudyal, D.R., Perera, K., 2023. Convolutional neural network-based deep learning approach for automatic flood mapping using NovaSAR-1 and Sentinel-1 data. ISPRS Int. J. Geo-Inf. 12, 194. https://doi.org/10.3390/ijgi12050194.

Arii, M., van Zyl, J.J., Kim, Y., 2010. A general characterization for polarimetric scattering from vegetation canopies. IEEE Trans. Geosci. Remote Sens. 48, 3349–3357. https://doi.org/10.1109/TGRS.2010.2046331.

Awad, M., Fraihat, S., 2023. Recursive feature elimination with cross-validation with decision tree: feature selection method for machine learning-based intrusion detection systems. J. Sens. Actuator Netw. 12, 67. https://doi.org/10.3390/jsan12050067.

Azad, R., Kazerouni, A., Azad, B., Khodapanah Aghdam, E., Velichko, Y., Bagci, U., Merhof, D., 2023. Laplacian-former: Overcoming the limitations of vision transformers in local texture detection. In: Greenspan, H., Madabhushi, A., Mousavi, P., Salcudean, S., Duncan, J., Syeda-Mahmood, T., Taylor, R. (Eds.), Medical Image Computing and Computer Assisted Intervention – MICCAI 2023. Springer Nature Switzerland, Cham, pp. 736–746.

Babu, A., Kumar, S., Agrawal, S., 2020. Polarimetric calibration of L-band UAVSAR data. J. Indian Soc. Remote Sens. 49, 541–549. https://doi.org/10.1007/s12524-020-01241-1.

Ballester-Berman, J.D., Lopez-Sanchez, J.M., 2010. Applying the Freeman–Durden decomposition concept to polarimetric SAR interferometry. IEEE Trans. Geosci. Remote Sens. 48, 466–479. https://doi.org/10.1109/TGRS.2009.2024304.

Banks, S., White, L., Behnamian, A., Chen, Z., Montpetit, B., Brisco, B., Pasher, J., Duffe, J., 2019. Wetland classification with multi-angle/temporal SAR using random forests. Remote Sens. 11, 670. https://doi.org/10.3390/rs11060670.

Bentivoglio, R., Isufi, E., Jonkman, S.N., Taormina, R., 2022. Deep learning methods for flood mapping: a review of existing applications and future research directions. Hydrol. Earth Syst. Sci. 2022, 1–50. https://doi.org/10.5194/hess-26-4345-2022.

Bhattacharya, A., Muhuri, A., De, S., Manickam, S., Frery, A.C., 2015. Modifying the Yamaguchi four-component decomposition scattering powers using a stochastic distance. IEEE J. Sel. Top. Appl. Earth Obs. Remote Sens. 8, 3497–3506. https://doi.org/10.1109/JSTARS.2015.2420683.

Blake, E.S., Zelinsky, D.A., 2018. Hurricane Harvey (Tropical Cyclone Report No. AL092017). National Hurricane Center, Miami, FL.

Brivio, P.A., Colombo, R., Maggi, M., Tomasoni, R., 2002. Integration of remote sensing data and GIS for accurate mapping of flooded areas. Int. J. Remote Sens. 23, 429–441. https://doi.org/10.1080/01431160010014729.

Brovelli, M.A., Sun, Y., Yordanov, V., 2020. Monitoring forest change in the Amazon using multi-temporal remote sensing data and machine learning classification on google earth engine. ISPRS Int. J. Geo-Inf. 9, 580. https://doi.org/10.3390/ijgi9100580.

Byun, J., Jun, C., Kim, J., Cha, J., Narimani, R., 2023. Deep learning-based rainfall prediction using cloud image analysis. IEEE Trans. Geosci. Remote Sens. 61, 1–11. https://doi.org/10.1109/TGRS.2023.3263872.

Callaghan, J., 2020. Extreme rainfall and flooding from Hurricane Florence. Trop. Cyclone Res. Rev. 9, 172–177. https://doi.org/10.1016/j.tcrr.2020.07.002.

Cantalloube, H., Nahum, C., 2000. How to compute a multi-look SAR image?, in: Proceedings of the CEOS SAR Workshop. European Space Agency, Toulouse, France, p. 635.

Cao, H., Zhang, H., Wang, C., Zhang, B., 2019. Operational flood detection using Sentinel-1 SAR data over large areas. Water 11, 786. https://doi.org/10.3390/w11040786.

Chapman, B., McDonald, K., Shimada, M., Rosenqvist, A., Schroeder, R., Hess, L., 2015. Mapping regional inundation with spaceborne L-band SAR. Remote Sens. 7, 5440–5470. https://doi.org/10.3390/rs70505440.

Chen, Y., Fan, R., Yang, X., Wang, J., Latif, A., 2018. Extraction of urban water bodies from high-resolution remote-sensing imagery using deep learning. Water 10, 585. https://doi.org/10.3390/w10050585.

Chen, Y., Zhang, L., Zou, B., Gu, G., 2023. Polarimetric SAR decomposition method based on modified rotational dihedral model. Remote Sens. 15, 101. https://doi.org/10.3390/rs15010101.

Chen, Z., Wang, C., Wang, Y., Jiang, G., Shen, Y., Tai, Y., Wang, C., Zhang, W., Cao, L., 2022. LCTR: on awakening the local continuity of transformer for weakly supervised object localization. In: In: Proceedings of the AAAI Conference on Artificial Intelligence, pp. 410–418. https://doi.org/10.1609/aaai.v36i1.19918.

Clement, M.A., Kilsby, C.G., Moore, P., 2018. Multi-temporal synthetic aperture radar flood mapping using change detection. J. Flood Risk Manag. 11, 152–168. https://doi.org/10.1111/jfr3.12303.

Cloude, S.R., Pottier, E., 1997. An entropy based classification scheme for land applications of polarimetric SAR. IEEE Trans. Geosci. Remote Sens. 35, 68–78. https://doi.org/10.1109/36.551935.

Cloude, S.R., Pottier, E., 1996. A review of target decomposition theorems in radar polarimetry. IEEE Trans. Geosci. Remote Sens. 34, 498–518. https://doi.org/10.1109/36.485127.

Colditz, R.R., 2015. An evaluation of different training sample allocation schemes for discrete and continuous land cover classification using decision tree-based algorithms. Remote Sens 7, 9655–9681. https://doi.org/10.3390/rs70809655.

Costa, M.P.F., 2004. Use of SAR satellites for mapping zonation of vegetation communities in the amazon floodplain. Int. J. Remote Sens. 25, 1817–1835. https://doi.org/10.1080/0143116031000116985.

Cui, Y., Yamaguchi, Y., Yang, J., Park, S.-E., Kobayashi, H., Singh, G., 2012. Three-component power decomposition for polarimetric SAR data based on adaptive volume scatter modeling. Remote Sens. 4, 1559–1572. https://doi.org/10.3390/rs4061559.

Dabboor, M., Shokr, M., 2023. Investigation of the sensitivity response of Touzi target scattering decomposition to modeled early ice growth. Int. J. Remote Sens. 44, 3456–3473. https://doi.org/10.1080/01431161.2023.2221803.

Dang, B., 2024. Comparison of polarization models in SAR technology for water body extraction (Master's thesis). KTH Royal Institute of Technology, Stockholm, Sweden.

Dormann, C.F., Elith, J., Bacher, S., Buchmann, C., Carl, G., Carré, G., Marquéz, J.R.G., Gruber, B., Lafourcade, B., Leitão, P.J., Münkemüller, T., McClean, C., Osborne, P.E., Reineking, B., Schröder, B., Skidmore, A.K., Zurell, D., Lautenbach, S., 2013. Collinearity: a review of methods to deal with it and a simulation study evaluating their performance. Ecography 36, 27–46. https://doi.org/10.1111/j.1600-0587.2012.07348.x.

Du, Z., Li, W., Zhou, D., Tian, L., Ling, F., Wang, H., Gui, Y., Sun, B., 2014. Analysis of Landsat-8 OLI imagery for land surface water mapping. Remote Sens. Lett. 5, 672–681. https://doi.org/10.1080/2150704X.2014.960606.

Duan, D., Wang, Y., Li, H., 2021. A descriptor to separate urban targets with large azimuth orientation angles from vegetation targets in PolSAR data. In: In: 2021 IEEE International Geoscience and Remote Sensing Symposium IGARSS. IEEE, pp. 5425–5428.

Edrich, M., 2004. Design overview and flight test results of the miniaturised SAR sensor MISAR, in: First European Radar Conference, 2004. EURAD. Presented at the First European Radar Conference, 2004. EURAD., European Microwave Association, Amsterdam, Netherlands, pp. 205–208.

Elkhrachy, I., 2022. Flash flood water depth estimation using SAR images, digital elevation models, and machine learning algorithms. Remote Sens. 14, 440. https://doi.org/10.3390/rs14030440.

Fayne, J.V., Bolten, J.D., Doyle, C.S., Fuhrmann, S., Rice, M.T., Houser, P.R., Lakshmi, V., 2017. Flood mapping in the lower Mekong River Basin using daily MODIS observations. Int. J. Remote Sens. 38, 1737–1757. https://doi.org/10.1080/01431161.2017.1285503.

Feaster, T.D., Weaver, J.C., Gotvald, A.J., Kolb, K., 2018. Preliminary peak stage and streamflow data for selected U.S. Geological Survey streamgaging stations in North and South Carolina for flooding following Hurricane Florence, September 2018 (U.S. Geological Survey Open-File Report No. 2018–1172). U.S. Geological Survey, Reston, VA.

Fore, A.G., Chapman, B.D., Hawkins, B.P., Hensley, S., Jones, C.E., Michel, T.R., Muellerschoen, R.J., 2015. UAVSAR polarimetric calibration. IEEE Trans. Geosci. Remote Sens. 53, 3481–3491. https://doi.org/10.1109/TGRS.2014.2377637.

Freeman, A., 2007. Fitting a two-component scattering model to polarimetric SAR data from forests. IEEE Trans. Geosci. Remote Sens. 45, 2583–2592. https://doi.org/10.1109/TGRS.2007.897929.

Freeman, A., Durden, S.L., 1998. A three-component scattering model for polarimetric SAR data. IEEE Trans. Geosci. Remote Sens. 36, 963–973. https://doi.org/10.1109/36.673687.

Freeman, A., Durden, S.L., 1993. Three-component scattering model to describe polarimetric SAR data, in: Radar Polarimetry. Presented at the Radar Polarimetry, SPIE, San Diego, CA, USA, pp. 213–224. Doi: 10.1117/12.140618.

Furtado, L.F. de A., Silva, T.S.F., Novo, E.M.L. de M., 2016. Dual-season and full-polarimetric C band SAR assessment for vegetation mapping in the Amazon *várzea* wetlands. Remote Sens. Environ. 174, 212–222. https://doi.org/10.1016/j.rse.2015.12.013.

Gorishniy, Y., Rubachev, I., Khrulkov, V., Babenko, A., 2023. Revisiting Deep Learning Models for Tabular Data. https://doi.org/10.48550/arXiv.2106.11959.

Gorishniy, Y., Rubachev, I., Khrulkov, V., Babenko, A., 2021. Revisiting deep learning models for tabular data, in: Advances in Neural Information Processing Systems. Curran Associates, Inc., pp. 18932–18943.

Guo, H., 2000. Spaceborne and airborne SAR for target detection and flood monitoring. Photogramm. Eng. Remote Sens. 66, 611–617.

Güvel, Ş.P., Akgül, M.A., Aksu, H., 2022. Flood inundation maps using Sentinel-2: a case study in Berdan Plain. Water Supply 22, 4098–4108. https://doi.org/10.2166/ws.2022.039.

Guyon, I., Weston, J., Barnhill, S., Vapnik, V., 2002. Gene selection for cancer classification using support vector machines. Mach. Learn. 46, 389–422. https://doi.org/10.1023/A:1012487302797.

Han, K., Jiang, M., Wang, M., Liu, G., 2018. Compact polarimetric SAR interferometry target decomposition with the Freeman–Durden method. IEEE J. Sel. Top. Appl. Earth Obs. Remote Sens. 11, 2847–2861. https://doi.org/10.1109/JSTARS.2018.2842125.

Han, P., Chen, Z., Wan, Y., Cheng, Z., 2020. Polsar image classification based on optimal feature and convolution neural network. In: IGARSS 2020–2020 IEEE International Geoscience and Remote Sensing Symposium. IEEE, Waikoloa, HI, USA, pp. 1735–1738. https://doi.org/10.1109/IGARSS39084.2020.9324670.

He, G., Feng, X., Xiao, P., Xia, Z., Wang, Z., Chen, H., Li, H., Guo, J., 2017. Dry and wet snow cover mapping in mountain areas using SAR and optical remote sensing data. IEEE J. Sel. Top. Appl. Earth Obs. Remote Sens. 10, 2575–2588. https://doi.org/10.1109/JSTARS.2017.2673409.

Huang, X., Reba, M., Coffin, A., Runkle, B.R.K., Huang, Y., Chapman, B., Ziniti, B., Skakun, S., Kraatz, S., Siqueira, P., Torbick, N., 2021. Cropland mapping with L-band UAVSAR and development of NISAR products. Remote Sens. Environ. 253, 112180. https://doi.org/10.1016/j.rse.2020.112180.

Humphrey Jr., C., Dillane, D., Iverson, G., O'Driscoll, M., 2021. Water table dynamics beneath onsite wastewater systems in eastern North Carolina in response to Hurricane Florence. J. Water Clim. Change 12, 2136–2146. https://doi.org/10.2166/wcc.2021.303.

James, G., Witten, D., Hastie, T., Tibshirani, R., Taylor, J., 2023. An introduction to statistical learning: with applications in Python, Springer Texts in Statistics. Springer International Publishing, Cham, 10.1007/978-3-031-38747-0.

Jet Propulsion Laboratory, 2015. PolSAR Data Format [WWW Document]. Uninhabited aerial vehicle synthetic aperture radar. URL https://uavsar.jpl.nasa.gov/science/documents/polsar-format.html (accessed 10.26.24).

Karim, F., Armin, M.A., Ahmedt-Aristizabal, D., Tychsen-Smith, L., Petersson, L., 2023. A review of hydrodynamic and machine learning approaches for flood inundation modeling. Water 15, 566. https://doi.org/10.3390/w15030566.

Kavats, O., Khramov, D., Sergieieva, K., 2022. Surface water mapping from SAR images using optimal threshold selection method and reference water mask. Water 14, 4030. https://doi.org/10.3390/w14244030.

Khosravi, K., Pham, B.T., Chapi, K., Shirzadi, A., Shahabi, H., Revhaug, I., Prakash, I., Bui, D.T., 2018. A comparative assessment of decision trees algorithms for flash flood susceptibility modeling at Haraz watershed, northern Iran. Sci. Total Environ. 627, 744–755. https://doi.org/10.1016/j.scitotenv.2018.01.266.

Kim, J.H., 2019. Multicollinearity and misleading statistical results. Korean J. Anesthesiol. 72, 558–569. https://doi.org/10.4097/kja.19087.

Krogager, E., 1990. New decomposition of the radar target scattering matrix. Electron. Lett. 18, 1525–1527. https://doi.org/10.1049/el:19900979.

Kuhn, M., Johnson, K., 2013. Applied predictive modeling. Springer, Berlin/Heidelberg, Germany.

LeCun, Y., Bengio, Y., Hinton, G., 2015. Deep learning. Nature 521, 436–444. https://doi.org/10.1038/nature14539.

Lee, J., Byun, J., Baik, J., Jun, C., Kim, H.-J., 2023. Estimation of raindrop size distribution and rain rate with infrared surveillance camera in dark conditions. Atmos. Meas. Tech. 16, 707–725. https://doi.org/10.5194/amt-16-707-2023.

Lee, J.-S., Pottier, E., 2017. Polarimetric radar imaging: from basics to applications. CRC Press, Boca Raton. https://doi.org/10.1201/9781420054989.

Li, N., Wang, R., Liu, Y., Du, K., Chen, J., Deng, Y., 2014. Robust river boundaries extraction of dammed lakes in mountain areas after Wenchuan Earthquake from high resolution SAR images combining local connectivity and ACM. ISPRS J. Photogramm. Remote Sens. 94, 91–101. https://doi.org/10.1016/j.isprsjprs.2014.04.020.

Li, Y., Yin, Q., Lin, Y., Hong, W., 2018. Anisotropy scattering detection from multiaspect signatures of circular polarimetric SAR. IEEE Geosci. Remote Sens. Lett. 15, 1575–1579. https://doi.org/10.1109/LGRS.2018.2850859.

Lian, W., Nie, G., Jia, B., Shi, D., Fan, Q., Liang, Y., 2020. An intrusion detection method based on decision tree-recursive feature elimination in ensemble learning. Math. Probl. Eng. 2020, 2835023. https://doi.org/10.1155/2020/2835023.

Liang, J., Liu, D., 2020. A local thresholding approach to flood water delineation using Sentinel-1 SAR imagery. ISPRS J. Photogramm. Remote Sens. 159, 53–62. https://doi.org/10.1016/j.isprsjprs.2019.10.017.

Liu, C., Yang, J., Ou, J., Fan, D., 2022. Offshore bridge detection in polarimetric SAR images based on water network construction using Markov tree. Remote Sens. 14, 3888. https://doi.org/10.3390/rs14163888.

Liu, Z., Huang, F., Li, L., Wan, E., 2002. Dynamic monitoring and damage evaluation of flood in north-west Jilin with remote sensing. Int. J. Remote Sens. 23, 3669–3679. https://doi.org/10.1080/01431160010006953.

Long, S., Fatoyinbo, T.E., Policelli, F., 2014. Flood extent mapping for Namibia using change detection and thresholding with SAR. Environ. Res. Lett. 9, 035002. https://doi.org/10.1088/1748-9326/9/3/035002.

Lou, Y., 2022. Uninhabited aerial vehicle synthetic aperture radar (UAVSAR) [WWW Document]. NASA Airborne Science Program. URL https://airbornescience.nasa.gov/instrument/UAVSAR (accessed 2.13.24).

M E, B.P., Kumar, S., 2020. PolInSAR decorrelation-based decomposition modelling of spaceborne multifrequency SAR data. Int. J. Remote Sens. 42, 1398–1419. https://doi.org/10.1080/01431161.2020.1829155.

Mahdianpari, M., Salehi, B., Mohammadimanesh, F., Motagh, M., 2017. Random forest wetland classification using ALOS-2 L-band, RADARSAT-2 C-band, and TerraSAR-X imagery. ISPRS J. Photogramm. Remote Sens. 130, 13–31. https://doi.org/10.1016/j.isprsjprs.2017.05.010.

Mahmoud, S.H., Gan, T.Y., 2018. Urbanization and climate change implications in flood risk management: developing an efficient decision support system for flood susceptibility mapping. Sci. Total Environ. 636, 152–167. https://doi.org/10.1016/j.scitotenv.2018.04.282.

Manavalan, R., 2017. SAR image analysis techniques for flood area mapping - literature survey. Earth Sci. Inform. 10, 1–14. https://doi.org/10.1007/s12145-016-0274-2.

Martinaitis, S.M., Cocks, S.B., Osborne, A.P., Simpson, M.J., Tang, L., Zhang, J., Howard, K.W., 2021. The historic rainfalls of Hurricanes Harvey and Florence: a perspective from the multi-radar multi-sensor system. J. Hydrometeorol. 22, 721–738. https://doi.org/10.1175/JHM-D-20-0199.1.

Martinez, J.-M., Le Toan, T., 2007. Mapping of flood dynamics and spatial distribution of vegetation in the Amazon floodplain using multitemporal SAR data. Remote Sens. Environ. 108, 209–223. https://doi.org/10.1016/j.rse.2006.11.012.

Martinis, S., Kersten, J., Twele, A., 2015. A fully automated TerraSAR-X based flood service. ISPRS J. Photogramm. Remote Sens. 104, 203–212. https://doi.org/10.1016/j.isprsjprs.2014.07.014.

Martinis, S., Rieke, C., 2015. Backscatter analysis using multi-temporal and multi-frequency SAR data in the context of flood mapping at River Saale, Germany. Remote Sens. 7, 7732–7752. https://doi.org/10.3390/rs70607732.

Matgen, P., Hostache, R., Schumann, G., Pfister, L., Hoffmann, L., Savenije, H.H.G., 2011. Towards an automated SAR-based flood monitoring system: lessons learned from two case studies. Phys. Chem. Earth a/b/c, Recent Advances in Mapping and Modelling Flood Processes in Lowland Areas 36, 241–252. https://doi.org/10.1016/j.pce.2010.12.009.

McNairn, H., Shang, J., 2016. A review of multitemporal synthetic aperture radar (SAR) for crop monitoring. In: Ban, Y. (Ed.), Multitemporal Remote Sensing: Methods and Applications. Springer International Publishing, Cham, pp. 317–340. https://doi.org/10.1007/978-3-319-47037-5_15.

Mehmood, H., Conway, C., Perera, D., 2021. Mapping of flood areas using Landsat with Google Earth Engine cloud platform. Atmosphere 12, 866. https://doi.org/10.3390/atmos12070866.

Melancon, A.M., Molthan, A.L., Griffin, R.E., Mecikalski, J.R., Schultz, L.A., Bell, J.R., 2021. Random forest classification of inundation following Hurricane Florence (2018) via L-band synthetic aperture radar and ancillary datasets. Remote Sens. 13, 5098. https://doi.org/10.3390/rs13245098.

Menard, S., 2001. Applied logistic regression analysis. SAGE Publications, Thousand Oaks, CA, USA.

Mohammadi, A., Costelloe, J.F., Ryu, D., 2017. Application of time series of remotely sensed normalized difference water, vegetation and moisture indices in characterizing flood dynamics of large-scale arid zone floodplains. Remote Sens. Environ. 190, 70–82. https://doi.org/10.1016/j.rse.2016.12.003.

Moharrami, M., Javanbakht, M., Attarchi, S., 2021. Automatic flood detection using Sentinel-1 images on the Google Earth Engine. Environ. Monit. Assess. 193, 248. https://doi.org/10.1007/s10661-021-09037-7.

Montgomery, D.C., Peck, E.A., Vining, G.G., 2021. Introduction to linear regression analysis. John Wiley & Sons, Hoboken, NJ, USA.

Morandeira, N.S., Grings, F., Facchinetti, C., Kandus, P., 2016. Mapping plant functional types in floodplain wetlands: an analysis of C-band polarimetric SAR data from RADARSAT-2. Remote Sens. 8, 174. https://doi.org/10.3390/rs8030174.

Moreira, A., Prats-Iraola, P., Younis, M., Krieger, G., Hajnsek, I., Papathanassiou, K.P., 2013. A tutorial on synthetic aperture radar. IEEE Geosci. Remote Sens. Mag. 1, 6–43. https://doi.org/10.1109/MGRS.2013.2248301.

Musa, Z.N., Popescu, I., Mynett, A., 2015. A review of applications of satellite SAR, optical, altimetry and DEM data for surface water modelling, mapping and parameter estimation. Hydrol. Earth Syst. Sci. 19, 3755–3769. https://doi.org/10.5194/hess-19-3755-2015.

NASA JPL, 2013. NASA Shuttle Radar Topography Mission Global 1 arc second. Doi: 10.5067/MEaSUREs/SRTM/SRTMGL1.003.

National Oceanic and Atmospheric Administration, 2024. Hurricane Florence flooding damage assessment images [WWW Document]. accessed 9.30.24. https://oceanservice.noaa.gov/news/sep18/florence-storm-imagery.html.

National Oceanic and Atmospheric Administration, 2017. Hurricane Harvey: emergency response imagery of the surrounding regions.

Nemni, E., Bullock, J., Belabbes, S., Bromley, L., 2020. Fully convolutional neural network for rapid flood segmentation in synthetic aperture radar imagery. Remote Sens. 12, 2532. https://doi.org/10.3390/rs12162532.

Neumann, M., 2009. Remote sensing of vegetation using multi-baseline polarimetric SAR interferometry: theoretical modeling and physical parameter retrieval. University of Rennes 1, Rennes, France. Doctoral dissertation.

O'brien, R.M., 2007. A caution regarding rules of thumb for variance inflation factors. Qual. Quant. 41, 673–690. https://doi.org/10.1007/s11135-006-9018-6.

Office of Marine and Aviation Operations, 2024. Beechcraft King Air 350/360CER [WWW Document]. accessed 9.30.24. https://www.omao.noaa.gov/aircraft-operations/aircraft/beechcraft-king-air-350360cer.

Otsu, N., 1979. A threshold selection method from gray-level histograms. IEEE Trans. Syst. Man Cybern. 9, 62–66.

Ouled Sghaier, M., Hammami, I., Foucher, S., Lepage, R., 2018. Flood extent mapping from time-series SAR images based on texture analysis and data fusion. Remote Sens. 10, 237. https://doi.org/10.3390/rs10020237.

Pallotta, L., Orlando, D., 2018. Polarimetric covariance eigenvalues classification in SAR images. IEEE Geosci. Remote Sens. Lett. 16, 746–750. https://doi.org/10.1109/LGRS.2018.2881485.

Pan, F., Xi, X., Wang, C., 2020. A comparative study of water indices and image classification algorithms for mapping inland surface water bodies using Landsat imagery. Remote Sens. 12, 1611. https://doi.org/10.3390/rs12101611.

Pham-Duc, B., Prigent, C., Aires, F., 2017. Surface water monitoring within Cambodia and the Vietnamese Mekong Delta over a year, with Sentinel-1 SAR observations. Water 9, 366. https://doi.org/10.3390/w9060366.

Phang, S.K., Chiang, T.H.A., Happonen, A., Chang, M.M.L., 2023. From satellite to UAV-based remote sensing: a review on precision agriculture. IEEE Access 11, 127057–127076. https://doi.org/10.1109/ACCESS.2023.3330886.

Pierdicca, N., Pulvirenti, L., Chini, M., 2018. Flood mapping in vegetated and urban areas and other challenges: models and methods. In: Refice, A., D'Addabbo, A., Capolongo, D. (Eds.), Flood Monitoring through Remote Sensing. Springer International Publishing, Cham, pp. 135–179. https://doi.org/10.1007/978-3-319-63959-8_7.

Plank, S., Jüssi, M., Martinis, S., Twele, A., 2017. Mapping of flooded vegetation by means of polarimetric Sentinel-1 and ALOS-2/PALSAR-2 imagery. Int. J. Remote Sens. 38, 3831–3850. https://doi.org/10.1080/01431161.2017.1306143.

Pottier, E., 2023. PolSARpro v6.0 (Biomass Edition).

Rahman, M.R., Thakur, P.K., 2018. Detecting, mapping and analysing of flood water propagation using synthetic aperture radar (SAR) satellite data and GIS: a case study from the Kendrapara District of Orissa State of India. Egypt. J. Remote Sens. Space Sci., EJRS Special Issue: Microwave Remote Sensing in Honor of Professor Adel Yehia 21, S37–S41. https://doi.org/10.1016/j.ejrs.2017.10.002.

Ramsey III, E., Rangoonwala, A., Bannister, T., 2013. Coastal flood inundation monitoring with satellite C-band and L-band synthetic aperture radar data. JAWRA J. Am. Water Resour. Assoc. 49, 1239–1260. https://doi.org/10.1111/jawr.12082.

Ramya, M.N.S., Kumar, S., 2021. PolInSAR coherence-based decomposition modeling for scattering characterization: a case study in Uttarakhand. India. Sci. Remote Sens. 3, 100020. https://doi.org/10.1016/j.srs.2021.100020.

Rättich, M., Martinis, S., Wieland, M., 2020. Automatic flood duration estimation based on multi-sensor satellite data. Remote Sens. 12, 643. https://doi.org/10.3390/rs12040643.

Razavi-Termeh, S.V., Seo, M., Sadeghi-Niaraki, A., Choi, S.-M., 2023. Flash flood detection and susceptibility mapping in the Monsoon period by integration of optical and radar satellite imagery using an improvement of a sequential ensemble algorithm. Weather Clim. Extremes 41, 100595. https://doi.org/10.1016/j.wace.2023.100595.

Richards, J.A., 2009. Interpretation based on structural models. In: Richards, J.A. (Ed.), Remote Sensing with Imaging Radar. Springer, Berlin/Heidelberg, Germany, pp. 281–301.

Richards, J.A., Woodgate, P.W., Skidmore, A.K., 1987. An explanation of enhanced radar backscattering from flooded forests. Int. J. Remote Sens. 8, 1093–1100. https://doi.org/10.1080/01431168708954756.

Rosen, P.A., Hensley, S., Wheeler, K., Sadowy, G., Miller, T., Shaffer, S., Muellerschoen, R., Jones, C., Madsen, S., Zebker, H., 2007. UAVSAR: new NASA airborne SAR system for research. IEEE Aerosp. Electron. Syst. Mag. 22, 21–28. https://doi.org/10.1109/MAES.2007.4408523.

Ross, K., 2018. Florence adds to woes of struggling water and sewer systems. Carolina Public Press.

Rubel, F., Kottek, M., 2010. Observed and projected climate shifts 1901-2100 depicted by world maps of the Köppen-Geiger climate classification. Meteorol. Z. 19, 135.

Saeys, Y., Inza, I., Larrañaga, P., 2007. A review of feature selection techniques in bioinformatics. Bioinformatics 23, 2507–2517. https://doi.org/10.1093/bioinformatics/btm344.

Saito, T., Rehmsmeier, M., 2015. The precision-recall plot is more informative than the ROC plot when evaluating binary classifiers on imbalanced datasets. PLoS One 10, e0118432.

Sayemuzzaman, M., Jha, M.K., 2014. Seasonal and annual precipitation time series trend analysis in North Carolina, United States. Atmos. Res. 137, 183–194. https://doi.org/10.1016/j.atmosres.2013.10.012.

Schumann, G., Bates, P.D., Apel, H., Aronica, G.T., 2018. Global flood hazard mapping, modeling, and forecasting. In: Schumann, G., Bates, P.D., Apel, H., Aronica, G.T. (Eds.), Global Flood Hazard. American Geophysical Union (AGU), pp. 239–244. https://doi.org/10.1002/9781119217886.ch14.

Schumann, G., Di Baldassarre, G., Alsdorf, D., Bates, P.D., 2010. Near real-time flood wave approximation on large rivers from space: application to the River Po. Italy. Water Resour. Res. 46. https://doi.org/10.1029/2008WR007672.

Sezgin, M., Sankur, B., 2004. Survey over image thresholding techniques and quantitative performance evaluation. J. Electron. Imaging 13, 146–165. https://doi.org/10.1117/1.1631315.

Shafai, S.S., Kumar, S., 2020. PolInSAR coherence and entropy-based hybrid decomposition model. Earth Space Sci. 7, e2020EA001279. https://doi.org/10.1029/2020EA001279.

Shultz, J.M., Galea, S., 2017. Mitigating the mental and physical health consequences of Hurricane Harvey. JAMA 318, 1437–1438. https://doi.org/10.1001/jama.2017.14618.

Singh, G., Malik, R., Mohanty, S., Rathore, V.S., Yamada, K., Umemura, M., Yamaguchi, Y., 2019. Seven-component scattering power decomposition of POLSAR coherency matrix. IEEE Trans. Geosci. Remote Sens. 57, 8371–8382. https://doi.org/10.1109/TGRS.2019.2920762.

Singh, G., Yamaguchi, Y., 2018. Model-based six-component scattering matrix power decomposition. IEEE Trans. Geosci. Remote Sens. 56, 5687–5704. https://doi.org/10.1109/TGRS.2018.2824322.

Singh, G., Yamaguchi, Y., Park, S.-E., 2013. General four-component scattering power decomposition with unitary transformation of coherency matrix. IEEE Trans. Geosci. Remote Sens. 51, 3014–3022. https://doi.org/10.1109/TGRS.2012.2212446.

Smith, A.B., 2025. 2024: An active year of U.S. billion-dollar weather and climate disasters. URL https://www.climate.gov/news-features/blogs/beyond-data/2024-active-year-us-billion-dollar-weather-and-climate-disasters (accessed 4.15.25).

Sokolova, M., Lapalme, G., 2009. A systematic analysis of performance measures for classification tasks. Inf. Process. Manag. 45, 427–437. https://doi.org/10.1016/j.ipm.2009.03.002.

Sommervold, O., Gazzea, M., Arghandeh, R., 2023. A survey on SAR and optical satellite image registration. Remote Sens. 15, 850. https://doi.org/10.3390/rs15030850.

Song, Y.-S., Sohn, H.-G., Park, C.-H., 2007. Efficient water area classification using Radarsat-1 SAR imagery in a high relief mountainous environment. Photogramm. Eng. Remote Sens. 73, 285–296. https://doi.org/10.14358/PERS.73.3.285.

Stewart, S., Berg, R., 2019. National hurricane center tropical cyclone report: hurricane florence. National Hurricane Center, National Oceanic and Atmospheric Administration, Miami, FL, USA.

Sun, Y., Huang, S., Li, J., Li, X., Ma, J., Qu, W., 2017. The downstream flood monitoring application of Myanmar Irrawaddy River based on Sentinel-1A SAR. Remote Sens. Technol. Appl. 32, 282–288.

Sun, Y., Lao, D., Ruan, Y., Huang, C., Xin, Q., 2023. A deep learning-based approach to predict large-scale dynamics of normalized difference vegetation index for the monitoring of vegetation activities and stresses using meteorological data. Sustainability 15, 6632. https://doi.org/10.3390/su15086632.

Swain, K.C., Singha, C., Nayak, L., 2020. Flood susceptibility mapping through the GIS-AHP technique using the cloud. ISPRS Int. J. Geo-Inf. 9, 720. https://doi.org/10.3390/ijgi9120720.

Sweet, W., Simon, S., Dusek, G., Marcy, D., Brooks, W., Pendleton, M., Marra, J., 2021. 2021 state of high tide flooding and annual outlook. Center for Operational Oceanographic Products and Services, National Ocean Service, National Oceanic and Atmospheric Administration, Silver Spring, MD.

Tarpanelli, A., Mondini, A.C., Camici, S., 2022. Effectiveness of Sentinel-1 and Sentinel-2 for flood detection assessment in Europe. Nat. Hazards Earth Syst. Sci. 22, 2473–2489. https://doi.org/10.5194/nhess-22-2473-2022.

Tellman, B., Sullivan, J.A., Kuhn, C., Kettner, A.J., Doyle, C.S., Brakenridge, G.R., Erickson, T.A., Slayback, D.A., 2021. Satellite imaging reveals increased proportion of population exposed to floods. Nature 596, 80–86. https://doi.org/10.1038/s41586-021-03695-w.

Thanh Noi, P., Kappas, M., 2018. Comparison of random forest, K-nearest neighbor, and support vector machine classifiers for land cover classification using Sentinel-2 imagery. Sensors 18, 18. https://doi.org/10.3390/s18010018.

Thornton, M.M., Shrestha, R., Wei, Y., Thornton, P.E., Kao, S.-C., 2022. Daymet: daily surface weather data on a 1-km grid for North America, version 4 R1. Doi: 10.3334/ORNLDAAC/2129.

Tong, X., Luo, X., Liu, S., Xie, H., Chao, W., Liu, S., Liu, S., Makhinov, A.N., Makhinova, A.F., Jiang, Y., 2018. An approach for flood monitoring by the combined use of Landsat 8 optical imagery and COSMO-SkyMed radar imagery. ISPRS J. Photogramm. Remote Sens. 136, 144–153. https://doi.org/10.1016/j.isprsjprs.2017.11.006.

Touzi, R., 2007. Target scattering decomposition in terms of roll-invariant target parameters. IEEE Trans. Geosci. Remote Sens. 45, 73–84. https://doi.org/10.1109/TGRS.2006.886176.

Tsai, Y.-L.-S., Dietz, A., Oppelt, N., Kuenzer, C., 2019. Remote sensing of snow cover using spaceborne SAR: a review. Remote Sens. 11, 1456. https://doi.org/10.3390/rs11121456.

Tsyganskaya, V., Martinis, S., Marzahn, P., Ludwig, R., 2018. SAR-based detection of flooded vegetation – a review of characteristics and approaches. Int. J. Remote Sens. 39, 2255–2293. https://doi.org/10.1080/01431161.2017.1420938.

Uddin, K., Matin, M.A., Thapa, R.B., 2021. Rapid flood mapping using multi-temporal SAR images: an example from Bangladesh. In: Bajracharya, B., Thapa, R.B., Matin, M.A. (Eds.), Earth Observation Science and Applications for Risk Reduction and Enhanced Resilience in Hindu Kush Himalaya Region. Springer International Publishing, Cham, pp. 201–210. https://doi.org/10.1007/978-3-030-73569-2_10.

Ullmann, T., Schmitt, A., Jagdhuber, T., 2016. Two component decomposition of dual polarimetric HH/VV SAR data: case study for the tundra environment of the Mackenzie Delta region, Canada. Remote Sens. 8, 1027. https://doi.org/10.3390/rs8121027.

U.S. Department of Agriculture, 2024. Landscape change monitoring system data explorer [WWW Document]. USDA Forest Service. URL https://apps.fs.usda.gov/lcms-viewer (accessed 8.8.24).

Van Zyl, J.J., 1993. Application of Cloude's target decomposition theorem to polarimetric imaging radar data. In: Radar Polarimetry. Presented at the Radar Polarimetry. SPIE, San Diego, CA, USA, pp. 184–191. https://doi.org/10.1117/12.140615.

Vaswani, A., Shazeer, N., Parmar, N., Uszkoreit, J., Jones, L., Gomez, A.N., Kaiser, Ł. ukasz, Polosukhin, I., 2017. Attention is all you need. In: Guyon, I., Luxburg, U.V., Bengio, S., Wallach, H., Fergus, R., Vishwanathan, S., Garnett, R. (Eds.), Advances in Neural Information Processing Systems. Curran Associates Inc.

Vatcheva, K., Lee, M., McCormick, J.B., Rahbar, M.H., 2016. Multicollinearity in regression analyses conducted in epidemiologic studies. Epidemiology 6, 227. https://doi.org/10.4172/2161-1165.1000227.

Verma, S., Kumar, S., Dsouza, H., 2023. Polarimetric decomposition and machine learning-based classification of L- and S-band airborne SAR (LS-ASAR) data. Earth Space Sci. 10, e2022EA002796. https://doi.org/10.1029/2022EA002796.

Vittinghoff, E., Glidden, D.V., Shiboski, S.C., McCulloch, C.E., 2012. Regression methods in biostatistics: linear, logistic, survival, and repeated measures models. Springer Science & Business Media, New York, NY, USA.

Wang, C., Pavelsky, T.M., Yao, F., Yang, X., Zhang, S., Chapman, B., Song, C., Sebastian, A., Frizzelle, B., Frankenberg, E., Clinton, N., 2022a. Flood extent mapping during Hurricane Florence with repeat-pass L-band UAVSAR images. Water Resour. Res. 58, e2021WR030606. https://doi.org/10.1029/2021WR030606.

Wang, J., Wang, S., Wang, F., Zhou, Y., Wang, Z., Ji, J., Xiong, Y., Zhao, Q., 2022b. FWENet: a deep convolutional neural network for flood water body extraction based on SAR images. Int. J. Digit. Earth 15, 345–361. https://doi.org/10.1080/17538947.2021.1995513.

Wang, J., Xiao, X., Qin, Y., Dong, J., Zhang, G., Kou, W., Jin, C., Zhou, Y., Zhang, Y., 2015. Mapping paddy rice planting area in wheat-rice double-cropped areas through integration of Landsat-8 OLI, MODIS and PALSAR images. Sci. Rep. 5, 10088. https://doi.org/10.1038/srep10088.

Wang, L., Xu, X., Yu, Y., Yang, R., Gui, R., Xu, Z., Pu, F., 2019. SAR-to-optical image translation using supervised cycle-consistent adversarial networks. IEEE Access 7, 129136–129149. https://doi.org/10.1109/ACCESS.2019.2939649.

Wang, Y., Imhoff, M.L., 1993. Simulated and observed L-HH radar backscatter from tropical mangrove forests. Int. J. Remote Sens. 14, 2819–2828. https://doi.org/10.1080/01431169308904311.

Waske, B., Braun, M., 2009. Classifier ensembles for land cover mapping using multitemporal SAR imagery. ISPRS J. Photogramm. Remote Sens., Theme Issue: Mapping with SAR: Techniques and Applications 64, 450–457. https://doi.org/10.1016/j.isprsjprs.2009.01.003.

White, L., Brisco, B., Dabboor, M., Schmitt, A., Pratt, A., 2015. A collection of SAR methodologies for monitoring wetlands. Remote Sens. 7, 7615–7645. https://doi.org/10.3390/rs70607615.

Woodhouse, I.H., 2017. Introduction to Microwave Remote Sensing. CRC Press, Boca Raton, FL, USA. https://doi.org/10.1201/9781315272573.

Wunnava, A., Naik, M.K., Panda, R., Jena, B., Abraham, A., 2020. An adaptive Harris hawks optimization technique for two dimensional grey gradient based multilevel image thresholding. Appl. Soft Comput. 95, 106526. https://doi.org/10.1016/j.asoc.2020.106526.

Xie, J., Li, Z., Zhou, C., Fang, Y., Zhang, Q., 2018a. Speckle filtering of GF-3 polarimetric SAR data with joint restriction principle. Sensors 18, 1533. https://doi.org/10.3390/s18051533.

Xie, Q., Meng, Q., Zhang, L., Wang, C., Wang, Q., Zhao, S., 2018b. Combining of the H/A/Alpha and Freeman–Durden polarization decomposition methods for soil moisture retrieval from full-polarization Radarsat-2 data. Adv. Meteorol. 2018, 9436438. https://doi.org/10.1155/2018/9436438.

Xu, B., Cui, Y., Zuo, B., Yang, J., Song, J., 2016. Polarimetric SAR image filtering based on patch ordering and simultaneous sparse coding. IEEE Trans. Geosci. Remote Sens. 54, 4079–4093. https://doi.org/10.1109/TGRS.2016.2536648.

Yamada, Y., 2001. Detection of flood-inundated area and relation between the area and micro-geomorphology using SAR and GIS, in: Scanning the Present and Resolving the Future. Presented at the IEEE 2001 International Geoscience and Remote Sensing Symposium (IGARSS 2001), Sydney, NSW, Australia, pp. 3282–3284. Doi: 10.1109/IGARSS.2001.978329.

Yamaguchi, Y., Moriyama, T., Ishido, M., Yamada, H., 2005. Four-component scattering model for polarimetric SAR image decomposition. IEEE Trans. Geosci. Remote Sens. 43, 1699–1706. https://doi.org/10.1109/TGRS.2005.852084.

Yamaguchi, Y., Sato, A., Boerner, W.-M., Sato, R., Yamada, H., 2011. Four-component scattering power decomposition with rotation of coherency matrix. IEEE Trans. Geosci. Remote Sens. 49, 2251–2258. https://doi.org/10.1109/TGRS.2010.2099124.

Yamaguchi, Y., Yajima, Y., Yamada, H., 2006. A four-component decomposition of POLSAR images based on the coherency matrix. IEEE Geosci. Remote Sens. Lett. 3, 292–296. https://doi.org/10.1109/LGRS.2006.869986.

Yamashita, R., Nishio, M., Do, R.K.G., Togashi, K., 2018. Convolutional neural networks: an overview and application in radiology. Insights Imaging 9, 611–629. https://doi.org/10.1007/s13244-018-0639-9.

Zhang, L., Zou, B., Cai, H., Zhang, Y., 2008. Multiple-component scattering model for polarimetric SAR image decomposition. IEEE Geosci. Remote Sens. Lett. 5, 603–607. https://doi.org/10.1109/LGRS.2008.2000795.

Zhang, S., Cui, L., Dong, Z., An, W., 2024. A deep learning classification scheme for PolSAR image based on polarimetric features. Remote Sens. 16, 1676. https://doi.org/10.3390/rs16101676.

Zhang, T., Wang, W., Yang, Z., Yin, J., Yang, J., 2021. Ship detection from PolSAR imagery using the hybrid polarimetric covariance matrix. IEEE Geosci. Remote Sens. Lett. 18, 1575–1579. https://doi.org/10.1109/LGRS.2020.3005683.

Zhang, W., Hu, B., Brown, G.S., 2020. Automatic surface water mapping using polarimetric SAR data for long-term change detection. Water 12, 872. https://doi.org/10.3390/w12030872.

Zhao, J., 2022. Large-scale flood mapping using SAR remote sensing data (Doctoral dissertation). Technische Universität Wien, Vienna, Austria. https://doi.org/10.34726/hss.2022.102580.

Zhao, Y., Jiang, M., 2022. Integration of optical and SAR imagery for dual PolSAR features optimization and land cover mapping. IEEE J. Miniatur. Air Space Syst. 3, 67–76. https://doi.org/10.1109/JMASS.2022.3195955.